Title

Enhancing and Extinguishing the Different Emission Features of 2D (EA

1âx

FA

x

)

4

Pb

3

Br

10

Perovskite Films

Authors

Kennard, Rhiannon M

Dahlman, Clayton J

Morgan, Emily E

et al.

Publication Date

2022-06-12

DOI

10.1002/adom.202200547

Peer reviewed

Enhancing and Extinguishing the Different Emission Features of Two-Dimensional $(EA_{1-x}FA_x)_4Pb_3Br_{10}$ Perovskite Films

*Rhiannon M. Kennard, † Clayton J. Dahlman, † Emily E. Morgan, †∞ Juil Chung, † Benjamin L. Cotts, # Joseph R. A. Kincaid, + Ryan A. DeCrescent, ‡ Kevin H. Stone, ▪ Shobhana Panuganti, ° Yahya Mohtashami, ‖ Lingling Mao, †∞ Richard D. Schaller, °≈ Alberto Salleo, # Mercouri G. Kanatzidis, ° Jon A. Schuller, ‖ Ram Seshadri, †∞+ Michael L. Chabinyc. †**

Rhiannon M. Kennard, Clayton J. Dahlman, Emily E. Morgan, Juil Chung, Lingling Mao, Ram Seshadri, and Michael L. Chabinyc *
† Materials Department, University of California, Santa Barbara, CA 93106, USA
*Email: mchabinyc@engineering.ucsb.edu

Emily E. Morgan, Lingling Mao, Ram Seshadri
∞ Materials Research Laboratory, University of California, Santa Barbara, CA 93106, USA

Joseph R. A. Kincaid, Ram Seshadri
+Department of Chemistry and Biochemistry, University of California, Santa Barbara, CA 93106, USA

Benjamin L. Cotts, Alberto Salleo
Department of Materials Science and Engineering, Stanford University, 496 Lomita Mall, Suite 102 Stanford, CA 94305, USA

Ryan A. DeCrescent
‡ Department of Physics, University of California, Santa Barbara, CA 93106, USA

Kevin H. Stone
▪ SSRL, SLAC National Accelerator Laboratory, Menlo Park, CA 94025, USA.

Shobhana Panuganti, Mercouri G. Kanatzidis, Richard D. Schaller
° Department of Chemistry, Northwestern University, Evanston, IL 60208, USA

≈ Richard D. Schaller
Center for Nanoscale Materials, Argonne National Laboratory, Lemont, IL 60439, USA

Yahya Mohtashami, Jon A. Schuller
‖ Department of Electrical and Computer Engineering, University of California, Santa Barbara,
CA 93106, USA

Keywords: 2D halide perovskite, emission, solvent, films, crystals, exciton-phonon coupling, self-trapped excitons

Abstract

Two-Dimensional (2D) hybrid perovskites are attractive for thin-film optoelectronic devices. However, in thin films, the color of optical emission and the texture of crystalline domains are often difficult to control. Here, a method for extinguishing or enhancing different emission features is demonstrated for the family of 2D Ruddlesden-Popper perovskites $(EA_{1-x}FA_x)_4Pb_3Br_{10}$ (EA = ethylammonium, FA = formamidinium). When grown from aqueous hydrobromic acid, crystals of $(EA_{1-x}FA_x)_4Pb_3Br_{10}$ retain all the emission features of their parent compound, $(EA)_4Pb_3Br_{10}$. Surprisingly, when grown from dimethylformamide (DMF), an emission feature, likely a p-like, self-trapped exciton, near 2.7 eV is missing. Extinction of this feature is correlated with DMF being incorporated between the 2D Pb-Br sheets, forming $(EA_{1-x}FA_x)_4Pb_3Br_{10}\cdot(DMF)_y$. Without FA, films grown from DMF form $(EA)_4Pb_3Br_{10}$, retain little solvent, and have strong emission near 2.7 eV. Separately, slowing the kinetics of film growth strengthens a different emission feature, likely a different type of self-trapped exciton, which is much broader and present in all compositions. Films of $(EA_{1-x}FA_x)_4Pb_3Br_{10}\cdot(DMF)_y$ have large, micron-sized domains and homogeneous orientation of the semiconducting sheets, resulting in low electronic disorder near the absorption edge. The ability to selectively strengthen or extinguish different emission features in films of $(EA_{1-x}FA_x)_4Pb_3Br_{10}\cdot(DMF)_y$ reveals a novel way to tune the emission color in these compounds.

1. Introduction

Two-dimensional (2D) perovskites are attractive for optoelectronic applications because their emission is tunable across the visible spectrum. [1–4] The Ruddlesden-Popper (RP) family of 2D perovskites have the structure $(A')_2(A)_{n-1}M_nX_{3n+1}$, where M is a metal (typically Pb or Sn), X is a halide (I, Cl, Br), A is a small cation that sits between the M-X octahedra, and A' is a larger cation (typically organic) that acts as a spacer for the 2D semiconducting A-M-X sheets. [3–9] The Dion-Jacobson (DJ) family is very similar, except the A' cation has two ammonium groups, which yields the structure $(A')(A)_{n-1}M_nX_{3n+1}$.[9] The emission color can be varied by changing the number of layers (n) of M-X octahedra in the semiconducting sheets, or by changing the halide between I, Br and Cl. While the emission of many 2D perovskites comes primarily from one narrow peak (a free exciton), [8,10] various mechanisms, such as coupling to phonons or defects, [11–13] can lead to additional emission at lower energies. Careful selection of A/A', M and X increases the distortions of the M-X bonds, which increases the intensity of these lower-energy emission features [13–19] and can broaden the emission until white. [15,20] The ease with which optical characteristics of free-standing 2D crystals can be tuned has rendered them attractive for light emitting devices, such as LEDs or lasers, and for light absorbing devices, such as solar cells or photodetectors. [3,21–28]

Thin film growth of 2D compounds has been heavily investigated for the development of optoelectronic devices. [21–25,29] Polycrystalline thin films are typically grown using solution-casting methods, [3] and unfortunately, such methods present several challenges. The first is that the composition of bulk 2D single crystals is often not retained in thin films.[30–32] In addition, the solvent and precursors can form different complexes in solution that can precipitate into highly-emissive impurities. [26,29–31,33–39] Finally, the orientation of the metal halide semiconducting layers relative to the substrate is difficult to control, particularly for 2D phases $(A')_2(A)_{n-1}M_nX_{3n+1}$ with $n > 1$. [3,32,37,40] Because the orientation of the semiconducting 2D layers determines the direction of carrier transport, controlling their orientation is crucial for optoelectronic applications. [3,21,24,37,40,41] Much research has focused on overcoming these challenges[30–32,34,37,42–54], with recent findings showing that that

judicious choice of precursor salts [50] and A/A' cations [52] can yield pure, single-phase films of 2D phases with $n > 1$.

Even when a film or crystal of an 2D phase is monophasic, the color of emission can vary. This variation in the emission spectra is not completely understood, and here we summarize current knowledge. In 2D perovskites, all of the emission occurs at energies smaller than the bandgap. Among these features, the free exciton emits at highest energy, followed by a variety of lower-energy features that arise from coupling of the free exciton to phonons or defects. These lower-energy features enable white-light emission, and provide avenues for fine-tuning the color of emission. [15,20] The origin of the lower-energy features is uncertain in many cases, with common assignments including types of exciton trapping, such as self-trapping and/or defect-mediated trapping. [12–19,55–62] Intriguingly, while the free exciton consistently appears in free-standing crystals and films of 2D phases, the lower-energy features do not consistently appear. For example, a specific lower-energy feature appears inconsistently in $(BA)_2PbI_4$ thin films across different studies, leading to conflicting explanations regarding its origins. [11,12,56,63,64] Lower-energy features can also vary in intensity across different locations of the same sample. [65] Recent work shows that film strain can be used to remove the lowest-energy feature of $(EA)_4Pb_3Br_{10}$. [52] In order to fully tune the emission color of 2D films, we must further explore how to change the optoelectronic properties of 2D phases using the film format.

Here, we show how the solvent impacts the lower-energy emission and morphology of films of a model 2D perovskite. We investigate a family of Ruddlesden-Popper compounds $(EA_{1-x}FA_x)_4Pb_3Br_{10}$, where EA is ethylammonium and FA is formamidinium. When grown from aqueous hydrobromic acid, crystals of $(EA_{1-x}FA_x)_4Pb_3Br_{10}$ retain all the emission features of their parent compound, $(EA)_4Pb_3Br_{10}$. Surprisingly, when grown from dimethylformamide (DMF), one specific emission feature, likely a p-like self-trapped exciton near 2.7 eV, is missing. In contrast with other studies, we show that small domain size is not the origin of the disappearance of this 2.7 eV emission. Spectroscopic and structural studies reveal that films without the emission at 2.7 eV have composition $(EA_{1-x}FA_x)_4Pb_3Br_{10}\cdot$DMF, with DMF located between the 2D Pb-Br sheets. The presence of DMF likely weakens

electron-phonon coupling that was responsible for the 2.7 eV emission. In addition, retention of DMF in thin films is correlated with large domain size, homogeneous orientation of crystallites and a steeper absorbance onset. We also find that slowing the growth kinetics of $(EA_{1-x}FA_x)_4Pb_3Br_{10}\cdot(DMF)_y$ films results in a larger proportion of a different low-energy emission feature. The ability to selectively extinguish different phonon-coupled emission features by solvent provides a novel way to tune the color of other 2D perovskites.

2. Results and Discussion

We aimed to find ways to control the proportions of different emission features in films in a 2D phase by varying its composition. We started from the $(EA)_4Pb_3Br_{10}$ composition, where EA is ethylammonium, because this phase exhibits three distinct emission features: one free exciton (FE), and two other features that arise from coupling of the free exciton to different phonon modes (hereafter called "phonon-coupled" features Ph-1 and Ph-2). [15,52] The structure of this n = 3 RP perovskite is shown in **Figure 1a**. [15] $(EA)_4Pb_3Br_{10}$ is unusual among halide perovskites, in that the A-site and spacer cations are identical. Solution growth of $(EA)_4Pb_3Br_{10}$ films is not plagued by competing crystallization of emissive impurities, in contrast to the challenging growth of films of mixed-cation 2D perovskites, such as the $(BA)_2(MA)_{n-1}Pb_nX_{3n+1}$, $(PEA)_2(MA)_{n-1}Pb_nX_{3n+1}$, or $(BDA)(MA)_{n-1}Pb_nX_{3n+1}$families. [29,30,32,37,50] We previously showed that $(EA)_4Pb_3Br_{10}$ can be easily cast as a single-phase, pure film. [52] Thus, $(EA)_4Pb_3Br_{10}$ is an ideal parent structure on which to test ways to control the proportions of different emission features. We also showed previously that strain from rapid casting suppresses broad emission in $(EA)_4Pb_3Br_{10}$, and that the intensity of broad emission is recovered by slowing the casting kinetics. [52] Such broad emission is thought to originate from self-trapped excitons (STEs) that might couple to a low-energy defect. [52] STE emission has been correlated with distortions to the inorganic structure: in an "ideal" lattice, such as cubic $MAPbBr_3$, the Pb-Br bond lengths are all equal and the bond angles are all 180°. However, the large size of cations such as EA (274 pm, [66,67]) in the A-site forces the Pb-Br bond lengths and angles away from these ideal values (**Figure 1a**) and can encourage formation of STEs. [15,17] We therefore investigated if replacing EA with a smaller cation would relieve these octahedral distortions, removing the conditions for STE emission and providing a way to tune the intensity of the phonon-coupled features.

2.1 Growth of Bulk Crystals of $(EA_{1-x}FA_x)_4Pb_3Br_{10}$

Before depositing the films, we first prepared powders from bulk crystals, in which the EA cation of $(EA)_4Pb_3Br_{10}$ was replaced by a smaller cation (**Figure 1**). We selected formamidinium (FA), which is slightly smaller than EA (253 pm for FA and 274 pm for EA [66,67]; **Figure 1a**-**1b**). Starting with a large cation and progressively changing composition with a smaller cation is the opposite approach to a common method where the initial cation is smallest. [68–70] EABr, FABr and $PbBr_2$ were weighed following the $(EA_{1-x}FA_x)_4Pb_3Br_{10}$ stoichiometry, and dissolved in hot aqueous hydrobromic acid $(HBr)_{aq}$. Large bulk crystals precipitated upon cooling (**Figure 1c**; see **Methods**), with dimensions on the order of hundreds of microns. The compositions refer to the stoichiometric amount of FA relative to EA *in the precursor solution,* $x_{FA,}$ and the resulting solid has approximately $(EA_{1-x}FA_x)_4Pb_3Br_{10}$ stoichiometry. The *actual* amount of FA in the $(EA_{1-x}FA_x)_4Pb_3Br_{10}$ stoichiometry was verified by NMR, and is designated $x_{FA,\ actual}$ (see **Figure S1**). The n = 3 designation means that the material has an n = 3 Ruddlesden-Popper structure and does not refer to the parent compound $(EA)_4Pb_3Br_{10}$ (x_{FA} = 0) specifically. For x_{FA} = 0, the structure formed was $(EA)_4Pb_3Br_{10}$, as previously verified. [15,52]

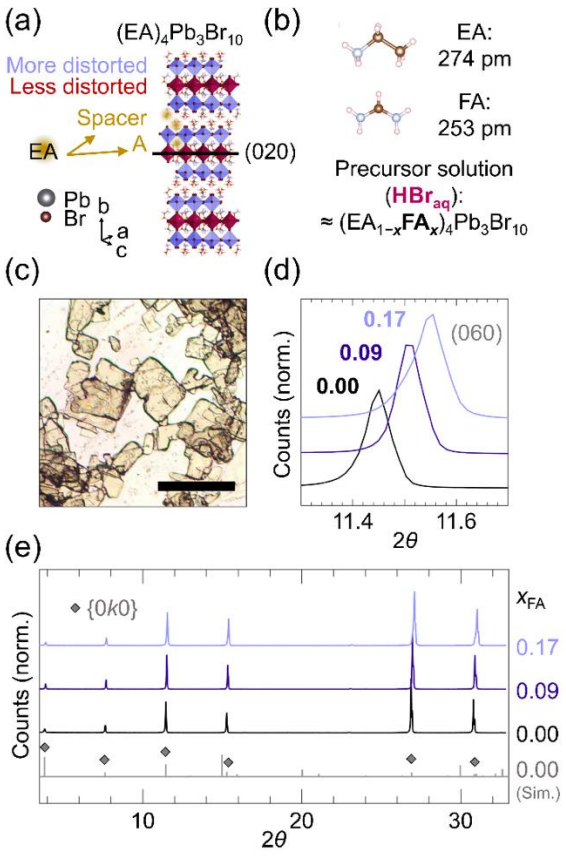

Figure 1. (a) Structure of $(EA)_4Pb_3Br_{10}$. The outer octahedra (blue) have more distorted Pb-Br bond lengths and angles; these are less distorted for the inner octahedra (red). EA is found in the A-site and spacer site. **(b)** Structures of EA and FA and their sizes. The stoichiometries of the precursor solutions made from hydrobromic acid are indicated. **(c)** Optical microscopy image of $(EA)_4Pb_3Br_{10}$ bulk crystals placed on a quartz substrate (scale bar: 500 μm). **(d)** X-Ray Diffraction (XRD) patterns of x_{FA} = 0.00, 0.09 and 0.17 bulk crystals placed on quartz substrates, focusing on the (060) peak, and showing a lattice contraction with increasing FA. **(e)** Full XRD patterns, with simulated XRD pattern of $(EA)_4Pb_3Br_{10}$, assuming no preferred crystallite orientation. The predominance of the signature (0*k*0) peaks reveals a preferred orientation of the bulk crystals on the substrate.

In bulk crystals, FA was successfully incorporated into n = 3 RP structures. The X-Ray Diffraction (XRD) patterns of powders from bulk crystals with x_{FA} = 0.00, 0.09 and 0.17 are shown in **Figure 1d**. Bulk crystals of $(EA)_4Pb_3Br_{10}$ (x_{FA} = 0.00) oriented on the substrate with the (0*k*0) peaks out-of-plane (i.e., 2D sheets parallel to the substrate), consistent with prior work. [52] As an example, the (020) plane is shown in **Figure 1a.** All (0*k*0) peaks are observed for x_{FA} = 0.09 and 0.17 indicating that an n = 3 structure is retained (**Figure 1e**). A slight lattice contraction is observed with increasing FA composition (**Figure 1d**), consistent with

FA being smaller than EA, and with no other changes occurring to the structure in crystals grown from $(HBr)_{aq}$. Individual bulk crystals of x_{FA} = 0.09 and 0.17 were selected for single crystal XRD analysis. The unit cells obtained for both x_{FA} = 0.09 and 0.17 show increasing shrinkage with increasing FA composition (see **Table S1** in the **Methods** for a brief description of the information obtained). However, a satisfactory structural model was not found due to disorder (see **Methods**). One possible explanation for this disorder is that FA can be located either in the A-site [71] or the spacer site.[72] We further verified FA incorporation into the n = 3 structures via NMR. [73] Bulk crystals of x_{FA} = 0.09 and 0.17 were dissolved in deuterated DMSO and the NMR spectra of the solutions confirmed the presence of both cations (**Figure S1**). NMR shows that the x_{FA} = 0.09 and 0.17 bulk crystals have $x_{FA,\ actual}$ = 0.03 and 0.08 respectively; the discrepancy possibly arises from different complexation of FA and EA in the precursor solution. Thus, FA is successfully incorporated into the n = 3 RP structures. 4

2.2 Emission features of $(EA_{1-x}FA_x)_4Pb_3Br_{10}$ bulk crystals

$(EA)_4Pb_3Br_{10}$ (x_{FA} = 0.00) bulk crystals have three emission features: a free exciton (FE) near 2.9 eV, and two features at lower energy, that arise from coupling of the free exciton to phonons (**Figure 2**). [52] We call these two features "Ph-1" and "Ph-2", for phonon-coupled 1 and 2. Ph-1 is narrow, and located near 2.7 eV, which is only 0.2 eV below the free exciton (see prior work for peak fits [52]). Moreover, the intensity of Ph-1 depends on measurement angle (**Figure S2**), and Ph-1 blue-shifts strongly with cooling.[52] These very particular characteristics suggest that Ph-1 is a self-trapped exciton (STE), which is p-like and associated with a magnetic dipole transition observed in similar materials.[12,56] In contrast, Ph-2 does not weaken with measurement angle (**Figure S2**), but does weaken with strain,[52] much like other broadband self-trapped excitons.[14,74] Thus, Ph-1 and Ph-2 are likely self-trapped excitons of different types.

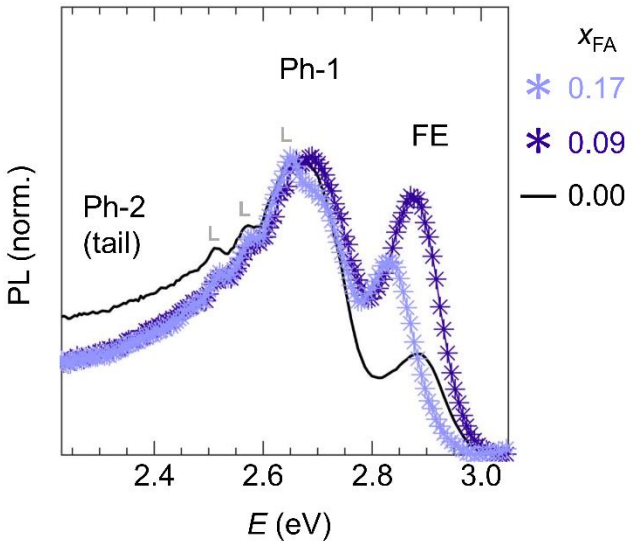

Figure 2. Photoluminescence (excitation 3.95 eV, 293 K) of x_{FA} = 0.00, 0.09 and 0.17 bulk crystals placed on quartz substrates. The free exciton (FE) is labelled, as are the two phonon-coupled features, Ph-1 and Ph-2, which are likely different types of self-trapped excitons. L designates features that are due to incomplete filtering of the excitation lamp by the monochromator used (see also **Figure S3**).

The three emission features of $(EA)_4Pb_3Br_{10}$ are all preserved after incorporation of FA. **Figure 2** shows photoluminescence from bulk crystals with x_{FA} = 0.00, 0.09 and 0.17. All three samples contain the free exciton, as well as Ph-1 and Ph-2. There is a slight red-shift of the free exciton with increasing FA, likely because the smaller FA cation in the A-site lowers the octahedral distortions relative to EA. [69] The relative intensities of the two phonon-coupled peaks, Ph-1 and Ph-2, do not change with incorporation of FA. Since phonon-coupled emission has been linked to octahedral distortions, [15,17] the octahedral distortions are likely still high. Overall, when grown from aqueous HBr, small amounts of FA in the n = 3 structure do not remove the phonon-coupled emission of $(EA_{1-x}FA_x)_4Pb_3Br_{10}$.

2.3 Drop-Cast Films of $(EA_{1-x}FA_x)_4Pb_3Br_{10}$·DMF and Origins of Ph-1 Weakening

We then investigated if changing the growth conditions of $(EA_{1-x}FA_x)_4Pb_3Br_{10}$ would change the optical properties of these phases. We weighed EABr, FABr and $PbBr_2$ in ratios corresponding to approximately $(EA)_4Pb_3Br_{10}$ (i.e., x_{FA} = 0.00) and $(EA_{0.93}FA_{0.07})_4Pb_3Br_{10}$ (i.e., x_{FA} = 0.07), and dissolved the EABr, FABr and $PbBr_2$ in DMF (see **Methods**). Hereafter, we focus on a low FA composition, x_{FA} = 0.07, due to the presence of additional phases at higher

FA compositions (**Figures S4**, **S5**, **S6**). The resulting solutions were drop-cast onto quartz substrates, and the solvent was left to evaporate for approximately 1h (all at 293 K). The films were subsequently annealed (373 K), and capped with a PMMA protective layer. We started with drop-casting, rather than spin-casting, because drop-casting preserves the emission features of the bulk crystals of $(EA)_4Pb_3Br_{10}$. [52] Drop-cast films with x_{FA} = 0.07 maintained the n = 3 structure, with the presence of strong (0k0) features in XRD ruling out intergrowth with other n phases (**Figure S7**). The crystallites were uniformly-oriented with Pb-Br sheets parallel to the substrate (**Figure S7**). For the drop-cast x_{FA} = 0.00, an n = 3 phase was also obtained, with Pb-Br sheets parallel to the substrate, consistent with prior work. [52] NMR revealed that the x_{FA} = 0.07 films had $x_{FA,\,actual}$ = 0.02, with the difference attributed to different complexation of FA and EA in solution (**Figure S8**). The composition obtained for films corresponds to a lower FA content than the bulk crystals made from aqueous HBr, which have $x_{FA,\,actual}$ = 0.03 and 0.08 respectively (for x_{FA} = 0.09 and 0.17 bulk crystals). While the FA content is slightly lower in films ($x_{FA,\,actual}$ = 0.02) than in bulk crystals ($x_{FA,\,actual}$ = 0.03), we believe that these FA contents are similar enough to compare properties.

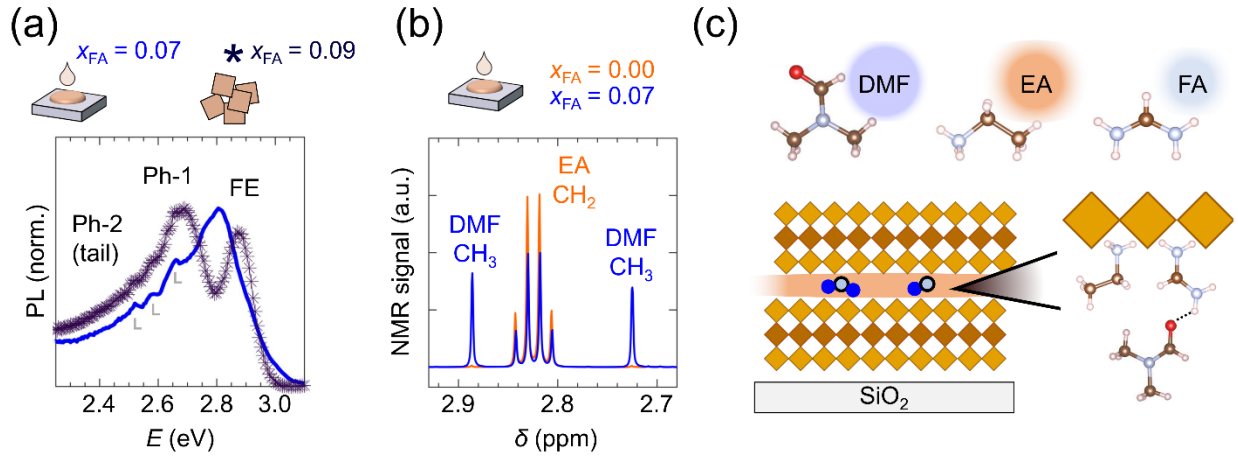

Figure 3. Retention of DMF when FA is present in $(EA_{1-x}FA_x)_4Pb_3Br_{10}$. **(a)** Photoluminescence of bulk crystals (x_{FA} = 0.09, $x_{FA,\,actual}$ = 0.03) made from aqueous HBr, and of a drop-cast and annealed film made from DMF (x_{FA} = 0.07, $x_{FA,\,actual}$ = 0.02). FE, Ph-1 and Ph-2 designate the free exciton and phonon-coupled features 1 and 2. Spectra were taken at excitation energy 3.95 eV and at 293 K. L designates features that are due to incomplete filtering of the excitation lamp by the monochromator used (see also **Figure S3**). **(b)** ^{1}H-NMR of drop-cast and annealed films with x_{FA} = 0.00 ($(EA)_4Pb_3Br_{10}$) and x_{FA} = 0.07 compositions prepared from DMF (no PMMA capping layer), that were then scraped off the substrates and dissolved in deuterated DMSO. See **Figure S8** for

full NMR analysis. **(c)** Schematic of the structure of x_{FA} = 0.07 films, and of hydrogen bonding between FA and DMF, but not between EA and DMF. For clarity, A-site cations are not shown.

Surprisingly, emission from the Ph-1 feature is weakened in the x_{FA} = 0.07 drop-cast films (**Figure 3a**). The photoluminescence of $(HBr)_{aq}$-made bulk crystals with similar x_{FA} (x_{FA} = 0.09) clearly shows all three features: the free exciton and phonon-coupled features Ph-1 and Ph-2. In contrast, the spectrum of the drop-cast film only has Ph-2 and the free exciton. The location of the free exciton is red-shifted; indeed, the free exciton gradually red-shifts in x_{FA} = 0.07 films prepared with different casting and annealing conditions (**Figure S7**, **S9**). We can eliminate a number of possible origins of the weakening of the Ph-1 feature: the weakening is not due to the presence FA alone, as the $(HBr)_{aq}$-made bulk crystals with FA substitution have strong emission at Ph-1 (**Figure 2**, **Figure 3a**). Drop-casting alone cannot be the source of the weakening, as drop-cast films of x_{FA} = 0.00 have a strong Ph-1 feature (**Figure S9** and prior work [52]). The weakening is also not an effect of small domain size, in contrast to other interpretations, [11] because the bulk crystals and drop-cast films have micron-sized domains, both laterally and vertically (**Figure 1c, S7**). We also verified that a weaker Ph-1 feature in the x_{FA} = 0.07 films is not an effect of measurement conditions that may change emission proportions, such as photoluminescence collection angle (**Figure S10**).

To determine why the Ph-1 feature weakens, we performed proton NMR on the drop-cast and annealed films of x_{FA} = 0.07 and x_{FA} = 0.00 (without the PMMA capping layer). We scraped these films off their substrates and dissolved the resulting powders in deuterated DMSO (**Figure 3b** – for discussion of 1H-NMR on spin-cast films see **Figure S8**). Notably, while both DMSO solutions contained NH_3 peaks from EA, the drop-cast x_{FA} = 0.07 sample additionally contained large DMF peaks. Weak FA peaks were also visible in the drop-cast x_{FA} = 0.00 sample. Peak integration shows that the ratio of EA: DMF: FA is 0.79: 0.19: 0.02 for drop-cast x_{FA} = 0.07, and that the ratio of EA: DMF is 0.998: 0.002 for drop-cast x_{FA} = 0.00 (**Figure S8**). We also acquired NMR spectra of the bulk crystals made from (HBr_{aq}). As expected, these contained peaks from EA and FA, but not DMF (**Figure S1**). Thus, the presence of DMF is correlated with weakened emission from Ph-1 (films of x_{FA} = 0.07), while the absence of DMF is correlated with strong emission from Ph-1 (bulk crystals of all x_{FA}, and

films of x_{FA} = 0.00). We therefore hypothesize that DMF influences the strength of emission from Ph-1.

We examined the n = 3 phases obtained in more detail to understand how DMF could influence the intensity of Ph-1. For drop-cast films of x_{FA} = 0.07, only an n = 3 phase is seen in XRD (**Figure S7**), but large amounts of DMF are seen via NMR (**Figure 3b**). DMF is therefore likely being incorporated into the n = 3 structure. The large size of DMF (≈ 300 pm) [75] prevents it from sitting in the A-site, so it is likely located between the Pb-Br sheets, near the spacer cations. Similar incorporation of solvent between M-X sheets via electrostatic interactions has been reported. [76] In addition, retention of DMF is facilitated by FA, as drop-cast x_{FA} = 0.00 films contain very little DMF (**Figure 3b**). It is likely that, when FA is located in the spacer site, the 2nd amino group of FA hydrogen bonds with the carbonyl group of DMF (**Figure 3c**), to form $(EA_{1-x}FA_x)_4Pb_3Br_{10}$·DMF, similar to FA_2PbBr_4-DMSO [77] or $(FA)_2Pb_3I_8$·4DMF. [78] In contrast, the sole amino group of EA is buried between the octahedra, and therefore ill-placed to make hydrogen bonds with DMF. Thus, the data are consistent with FA in the spacer site retaining DMF.

The structural changes induced by DMF likely remove conditions necessary for emission at 2.7 eV. Prior work shows that the feature at 2.7 eV (Ph-1) behaves like it is coupled to a phonon. [52] Phonon-coupled emission is sensitive to both the spatial arrangement [79,80] and dynamics [80,81] of the cations in the interlayer. DMF in the interlayer should modify how the spacer cations are arranged (**Figure 3c**), and could relieve specific Pb-Br octahedral distortions. Such a relief might weaken exciton-phonon interactions specific to Ph-1. Relief of the octahedral distortions can also explain why for similar x_{FA}, the free exciton of the drop-cast film is at lower energy than the free exciton of bulk crystals. [69] In addition, H-bonding interactions between DMF and the FA spacer cation may 1) change the interactions of FA and octahedral bromides due to charge shielding/withdrawing effects, or 2) affect octahedral tilting modes that couple with an STE. These effects could make the octahedral network stiffer and lessen the self-trapping. Alternately, such effects could change the energy of phonon modes away from coupling overlap with the free exciton.

[61,81,82] Thus, DMF in the interlayer likely interferes with carrier-phonon processes responsible for Ph-1.

2.4 Growth of Spin-Cast Films with FA and MA Substitution

Next, we investigated how such effects manifest in spin-cast films, which is the most common method used to cast metal halide perovskite films. We used Grazing Wide-Angle X-Ray Scattering (GIWAXS) to compare the structure of films of x_{FA} = 0.07 to that of x_{FA} = 0.00 reported previously. A simulated GIWAXS pattern of $(EA)_4Pb_3Br_{10}$ with uniform orientation of 2D sheets parallel to the substrate is shown in **Figure 4b** (reproduced with permission from prior work [52]). On this simulated pattern, the (0*k*0) peaks of the *n* = 3 phase corresponding to stacking of the Pb-Br sheets are labelled. Prior work from our group demonstrated that spin-casting the x_{FA} = 0.00 composition yields phase-pure films of $(EA)_4Pb_3Br_{10}$. [52] The x_{FA} = 0.00 film has (0k0) peaks/Pb-Br sheets oriented both parallel and perpendicular to the substrate. The GIWAXS peaks of $(EA)_4Pb_3Br_{10}$ are also ring-like, signaling disorder in sheet stacking with respect to q_Z and q_{XY}. Correspondingly, Scanning Electron Microscopy (SEM, **Figure 5a**) reveals small domains and many pinholes for the x_{FA} = 0.00 film. While the $(EA)_4Pb_3Br_{10}$ film is monophasic, it is desirable for the domain sizes to be larger, with more uniform orientation for many applications.

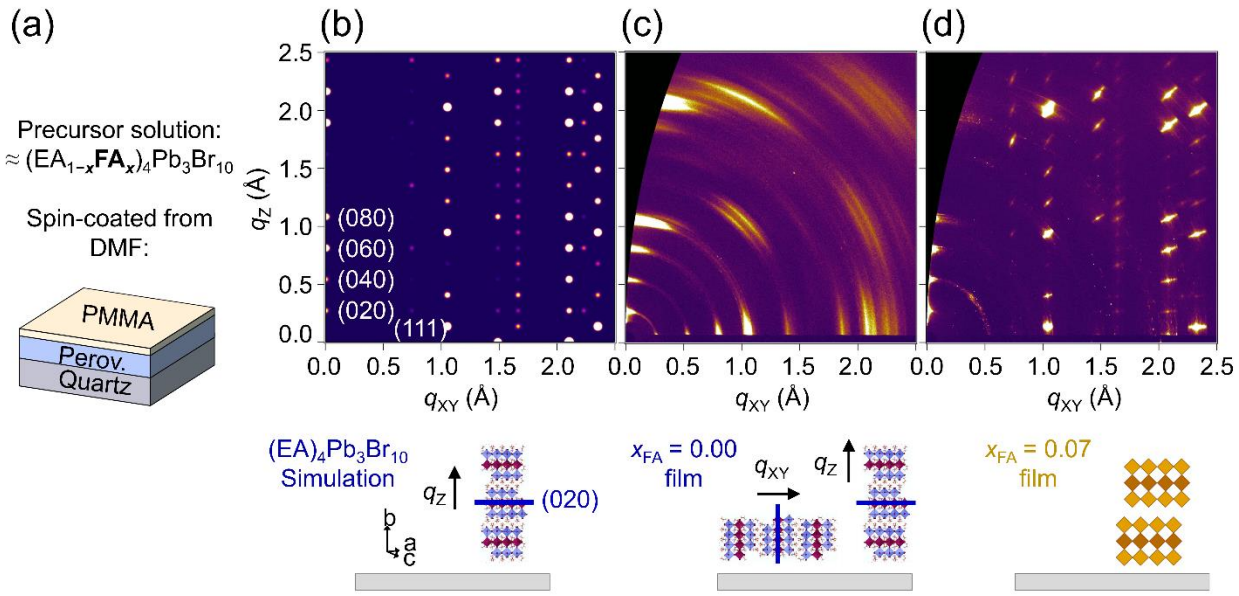

Figure 4. (a) Schematic of spin-cast film preparation from DMF precursor solution. **(b)** Simulation of the GIWAXS pattern for $(EA)_4Pb_3Br_{10}$, assuming that all crystallites have semiconducting sheets parallel to the substrate. The main (0*k*0) peaks are indexed, as well as the (111). **(c)-(d)** GIWAXS patterns of spin-cast films of **(c)** x_{FA} = 0.00 ($(EA)_4Pb_3Br_{10}$) and **(d)** x_{FA} = 0.07. Panels **(b)** and **(c)** are reproduced with permission from reference [52]; Copyright 2021, Rhiannon M. Kennard, Clayton J. Dahlman, Juil Chung, et al., published by ACS (Chemistry of Materials).

In contrast to the EA-only films, FA substitution produced spin-cast films with large, homogeneously oriented domains. GIWAXS from the spin-cast x_{FA} = 0.07 films shows similar locations to those of the simulated pattern of $(EA)_4Pb_3Br_{10}$, which assumed perfect orientation of the sheets parallel to the substrate (**Figure 4**). The GIWAXS reveals (1) that the x_{FA} = 0.07 film has an n = 3 structure in bulk, and (2) that the semiconducting sheets of spin-cast x_{FA} = 0.07 are uniformly oriented parallel to the substrate. There is a weaker feature near 0.5 $Å^{-1}$ (see **Figure S4**, **S11**) that does not belong to the n = 3 phase, but the film is predominantly n = 3. In addition, the lattice spacings of x_{FA} = 0.00 and 0.07 films are similar (**Figures S4**, **S11**). The diffraction peaks are sharp for x_{FA} = 0.07, further indicating good orientational uniformity. Scanning electron microscopy (SEM) showed that the spin-cast films of x_{FA} = 0.07 and x_{FA} = 0.00 had comparable thickness, but the x_{FA} = 0.07 films had an order-of-magnitude increase in lateral domain size, and disappearance of pinholes (**Figure 5b**). Consistently, the XRD and GIWAXS peaks of x_{FA} = 0.07 are narrower than those of x_{FA} = 0.00 (**Figure S4**, **S11**), likely due to the increase in domain size. Thus, adding FA to the DMF precursor solution yields spin-cast films that have an n = 3 phase, large domains, and homogeneous orientation of the 2D sheets.

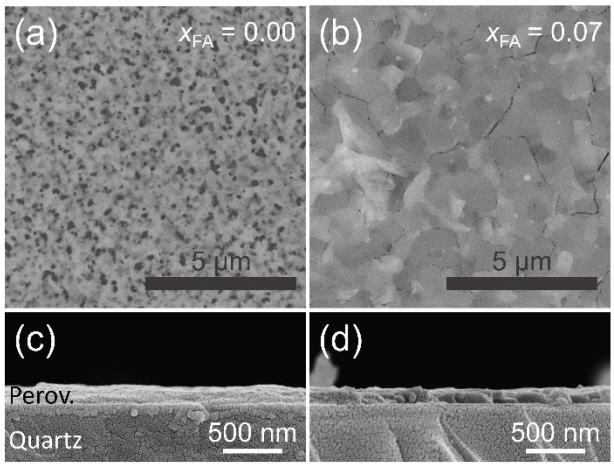

Figure 5. SEM images of films spin-cast from DMF with compositions **(a)-(c)** x_{FA} = 0.00 ($(EA)_4Pb_3Br_{10}$) and **(b)-(d)** x_{FA} = 0.07. Films were not coated with PMMA for SEM experiments, to best image the perovskite domains. For the cross-sections, spin-cast films were cut in half with a diamond scribe, which likely induced some fracturing. However, even in cross-sectional SEM (**(c)-(d)**), the x_{FA} = 0.07 spin-cast film appears to have more defined domains than the x_{FA} = 0.00 film.

FTIR and XRD show that spin-cast films incorporate less DMF than drop-cast films of the same x_{FA} = 0.07 composition. We tried to determine the amount of DMF present in spin-cast films via solution NMR, but the limited mass of the sample led to uncertainty in the composition (see discussion of **Figure S8**). We therefore turned to Fourier Transform Infrared Spectroscopy (FTIR) to determine the composition (**Figure S12**). The FTIR spectra shows a weak peak at 1705 cm^{-1} consistent with the C=N stretch of FA. No clear feature at lower wavenumber is attributable to DMF, indicating that if DMF is present then the concentration must be lower than that of FA. In contrast, DMF is observed via NMR in drop-cast x_{FA} = 0.07 films (**Figure 3b**). XRD shows that the spacing between Pb-Br sheets is smaller in spin-cast films than in drop-cast films of x_{FA} = 0.07 (see XRD of **Figure S7**), again suggesting that spin-cast films of x_{FA} = 0.07 incorporate less DMF. This presence of DMF complicates strain analysis of thin films, because the spacings of the (0k0) in drop-cast films of x_{FA} = 0.07 cannot be taken as the spacings of the unstrained lattice. Spin-cast x_{FA} = 0.00 film contains small strains, [52] and it is likely that the spin-cast x_{FA} = 0.07 do as well. Thus, the amount of DMF seems to vary with growth kinetics.

The growth of large, homogeneously-oriented domains in spin-cast x_{FA} = 0.07 may originate from the interactions of DMF and FA in the precursor solution (**Figure 4**, **Figure 5**). First, DMF does not need to fully leave the interlayer for the x_{FA} = 0.07 composition to form an n = 3 phase, so 2D sheets can grow more easily than for the EA-only composition. The easiest growth direction for the 2D sheets is parallel to the substrate, so large domains are formed with uniform sheet orientation parallel to the substrate. However, it is also possible that the presence of DMF in the interlayer is not the origin of the large and uniform growth. Rather, DMF and FA together could act as surfactants or help the formation of an n = 3 "seed" in the precursor solution that result in large and homogeneously-oriented domains. [48,50] The N-H group of FA in the interlayer can form hydrogen bonds with DMF, resulting in DMF incorporation into the interlayer of an n = 3. Thus, the large, homogeneously oriented domains of the spin-cast x_{FA} = 0.07 film likely originate from the interactions of DMF and FA in the precursor solution.

We also examined whether these interactions are specific to FA and DMF, to determine if cations could interact with DMF to produce the changes to emission and morphology seen in $(EA_{1-x}FA_x)_4Pb_3Br_{10}$·DMF. We therefore repeated the spin-casting experiments, but with precursors solutions of stoichiometry $(EA_{1-x}MA_x)_4Pb_3Br_{10}$, where MA is methylammonium. Neither the increases to domain size nor the extinction of Ph-1 are observed (**Figure S13**). This result is likely because MA is located in the A-site, and may be less likely to retain DMF in the interlayer. In addition, MA is also less likely to hydrogen bond with DMF, as it only has one N-H group, like EA. Thus, the simultaneous choice of organic cation (EA, FA, MA) and solvent (DMF, HBr_{aq}) seems to dictate the strength of emission from Ph-1 and film morphology.

2.5 Optical Properties of Spin-Cast Films of $(EA_{1-x}FA_x)_4Pb_3Br_{10}$·DMF

Photoluminescence measurements reveal an obvious extinction of the Ph-1 feature in spin-cast films in compositions with FA (**Figure 6**). Emission from the spin-cast x_{FA} = 0.00 film contains the free exciton (FE), and both phonon-coupled emission features: Ph-1 and Ph-2. In contrast, emission from the spin-cast x_{FA} = 0.07 film is missing Ph-1 (**Figure 6**; see **Figure S5** for spectra over a greater energy range). The presence of Ph-1 in the x_{FA} = 0.00 films,

which have small lateral and vertical domains (< 200 nm), suggests that small domain size does not remove Ph-1. Moreover, the removal of Ph-1 in films of x_{FA} = 0.07, which have larger lateral domains than films of x_{FA} = 0.00 (**Figure 5**), further confirms that the removal of Ph-1 is not an effect of small domain size, as proposed elsewhere. [11] The behavior of Ph-2 in FA-containing compounds is consistent with prior work on $(EA)_4Pb_3Br_{10}$: [52] the intensity of Ph-2 increases when the growth kinetics are slow (in drop-cast films, bulk crystals - see **Figure 2, S9**), and decreases when the growth kinetics are fast (spin-cast films). This decrease is previously attributed to strains acquired during the rapid spin-casting, that hinder emission from Ph-2. [52] Thus, Ph-1 is weakened for x_{FA} films made from DMF, independently of film thickness and growth kinetics.

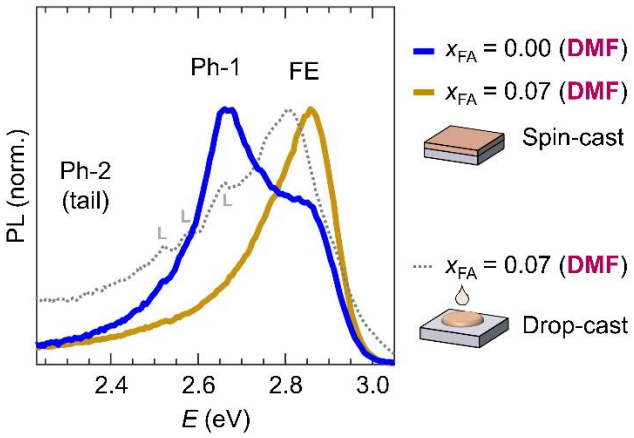

Figure 6. Photoluminescence (PL) of spin-cast and drop-cast films (with annealing) with precursor solutions x_{FA} = 0.07and x_{FA} = 0.00 ($(EA)_4Pb_3Br_{10}$), with excitation 3.95 eV at 293 K. The solvent is labelled (DMF). Emission features are labelled as free excitons (FE) and phonon-coupled emission features 1 and 2 (Ph-1 and Ph-2). For additional comparisons of PL of samples grown in different ways, see **Figure S9**. L designates features that are due to incomplete filtering of the excitation lamp by the monochromator used (see also **Figure S3**). An explanation of why scattering is observed more in some samples than others can be found below **Figure S3**.

The weakening of Ph-1 and Ph-2 reveals new ways to tune emission in films. It is interesting that Ph-1 is weakened, but that the low-energy phonon-coupled tail, Ph-2, is retained in drop-cast films of x_{FA} = 0.07 (**Figure 6**). This difference suggests that Ph-1 and Ph-2 are coupled to different phonon modes. Thus, film growth can provide novel routes to selectively extinguish different emission features: DMF and FA can extinguish one emission feature, and growth kinetics can weaken another. [52] This type of tuning is especially

interesting because it is often unavailable to bulk crystal synthesis. The extinction observed here is also unusual. While solvent incorporation can gradually shift the energy of the free exciton, [77] extinction of a self-trapped exciton due to solvent incorporation in a crystalline structure has not been reported to our knowledge. These results also show that care must be taken when studying optical processes because the growth method or solvents may enhance or suppress different emission features. Such variations might explain why lower-energy features appear inconsistently across a sample of $(PDMA)PbI_4$, [65] or from study to study in $(BA)_2PbI_4$. [11,12,56]

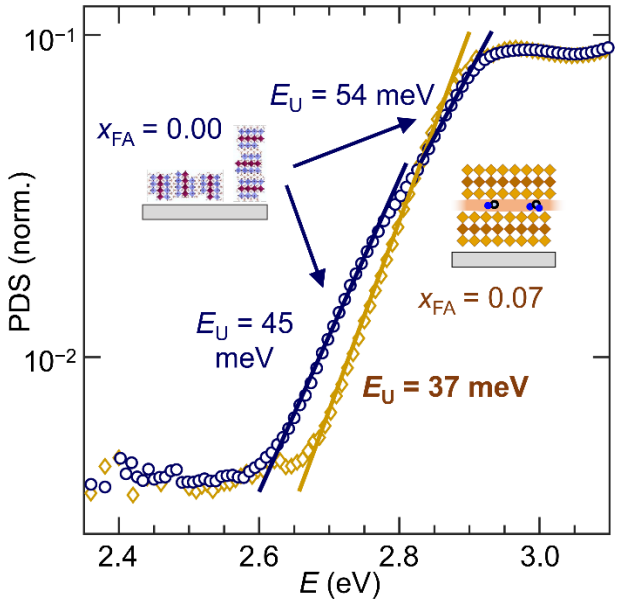

Figure 7. PDS spectra of spin-cast films of x_{FA} = 0.00 ($(EA)_4Pb_3Br_{10}$) and x_{FA} = 0.07, showing fits of different absorption onsets and their respective Urbach energies E_U. For goodness of fits see the **Section S2: Fitting the PDS Data**.

Finally, because a sharp absorbance onset is highly desired for photovoltaics and photodetectors, we measured the electronic disorder near the absorption edge. **Figure 7** shows Photothermal Deflection Spectroscopy (PDS) analysis of the absorbance onsets of spin-cast films of x_{FA} = 0.00 ($(EA)_4Pb_3Br_{10}$) and x_{FA} = 0.07, throughout the < 200 nm film thickness (**Figure 5**). Onsets were fit (see **Section S2: Fitting the PDS Data**) in order to extract the Urbach energies E_U, which represents the degree of electronic disorder near the absorption edge. As discussed previously, [52] the $(EA)_4Pb_3Br_{10}$ film has two absorbance

onsets, with high Urbach energies, of 45 meV and 54 meV. These two onsets likely correspond to the two crystallite types in the film (crystallites with 2D sheets parallel vs. perpendicular to the substrate), that each exhibit different strain. Indeed, the energy of the free exciton can be shifted by small strains, [83] like those present in the film. [52] The two PDS onsets do not originate from the free exciton and Ph-1: unstrained bulk crystals of $(EA)_4Pb_3Br_{10}$ have only one onset in this region, but contain both the free exciton and Ph-1. [52] The presence of only one onset near 2.6-2.8 eV in bulk crystals of $(EA)_4Pb_3Br_{10}$ thus confirms that Ph-1 does not originate from a defect that weakly absorbs at lower energies. [13] The high Urbach energies of the two onsets in x_{FA} = 0.00 (45 meV and 54 meV) likely arise from strain and morphology-induced disorder.

In contrast, the spin-cast x_{FA} = 0.07 film has a single absorbance onset, with much lower Urbach energy of 37 meV. This improvement in the absorbance onset is so pronounced that it is also weakly visible via UV-Vis (**Figure S5**). The single absorbance onset of x_{FA} = 0.07 likely stems from uniform crystallite orientation (**Figure 4**), as the homogeneous orientation likely means that the crystallites only experience one type of strain. Because we do not have an unstrained reference for the spin-cast x_{FA} = 0.07 film (see above), we cannot confirm the strain it experiences to verify how this strain might affect the absorbance onset. However, the x_{FA} = 0.07 film likely has strain that arises from spin-casting, [52,84] as it is has less Ph-2 than drop-cast x_{FA} = 0.07 (**Figure 6**). The low Urbach energy likely originates from increases in domain size and lack of pinholes (**Figure 5**). It is also possible that DMF in the interlayer relieves octahedral distortions inherent to the $(EA)_4Pb_3Br_{10}$ phase, such that even though x_{FA} = 0.07 films exhibit strain from spin-casting/annealing, the electronic disorder is much lower in x_{FA} = 0.07 films than in $(EA)_4Pb_3Br_{10}$ films. Overall, the x_{FA} = 0.07 film has a very sharp absorbance onset, which is highly desirable for optoelectronic devices such as photodetectors or photovoltaics. [85]

3. Conclusions

We have demonstrated that the optical emission and morphology in films of two-dimensional hybrid perovskites is modified by solvent and growth conditions. Adding FA to

the precursor solution of $(EA_{1-x}FA_x)_4Pb_3Br_{10}$ films leads to retention of DMF in between the semiconducting sheets to form $(EA_{1-x}FA_x)_4Pb_3Br_{10}{\cdot}DMF_y$; and this solvent retention is not observed when using aqueous HBr. The use of DMF as a solvent for casting thin films is correlated with large domain size, homogeneous texture of the crystallites, disappearance of pinholes, decrease in electronic disorder near the absorbance onset, and most interestingly, the complete extinction of a lower-energy emission feature (likely a p-like self-trapped exciton) in spin-cast films. We show that small lateral or vertical domain size, implicated in prior studies, cannot be the origin of the disappearance of this emission, as this feature is weakened even in films whose domains are microns wide and thick. Possible reasons for this weakening include different cation stacking in the interlayer, relief of Pb-Br octahedral distortions, changes to interactions between cations and $PbBr_6$ octahedra, and changes to their tilting modes. To our knowledge, this is the first report of incorporated solvent extinguishing a lower-energy emission feature in a halide perovskite structure. The potential for residual solvent to weaken a self-trapped exciton could also explain why lower-energy features appear inconsistently across different studies or in different locations of the same sample. If an emission feature is unexpectedly weak in films, the films should be checked if solvent is incorporated into the structure. We also show that slowing the growth kinetics of $(EA_{1-x}FA_x)_4Pb_3Br_{10}$ films increases the proportion of a second low-energy emission feature, consistent with our prior work on $(EA)_4Pb_3Br_{10}$ films. The ability to selectively extinguish different phonon-coupled emission features is demonstrated for $(EA_{1-x}FA_x)_4Pb_3Br_{10}{\cdot}(DMF)_y$ films, and may provide novel ways to tune the color of other 2D perovskites.

4. Experimental Section/Methods

Materials Lead bromide ($PbBr_2$, 99.999 %), ethylammonium bromide (EABr, ≥ 98 %), lead oxide (PbO, ≥ 99.0 %), methylammonium bromide (MABr, 98 %), N-N-dimethylformamide (DMF, 99.8%, anhydrous), poly (methyl methacrylate) (PMMA, MW 350000), and hydrobromic acid (HBr, ACS reagent, 48%), deuterated DMSO (Dimethyl sulfoxide-d_6, 99.9 % atom D, in ampules of 650 µL) were purchased from Sigma Aldrich and used as received. Two precursors were used for formamidinium bromide (FABr). One FABr precursor was purchased from Sigma Aldrich (≥ 98 %); and the second was made following a reported procedure. [86] Briefly, formamidine acetate (99 %, Sigma Aldrich)

was dissolved in ethanol, and aqueous hydrobromic acid was added in excess with respect to FA. The mixture was left to stir in air for > 1h. The solvent was then roto-vaped off, and the resulting solids were washed multiple times with diethyl ether. The product was vacuum dried overnight. Fourier Transform Infrared Spectroscopy (FTIR) was used to confirm complete conversion of formamidine acetate to FABr (data not shown). The FABr from Sigma Aldrich and the home-synthesized FABr both yielded spin-cast films of x_{FA} = 0.07 ($(EA_{0.93}FA_{0.07})_4Pb_3Br_{10}$) with identical XRD patterns and photoluminescence (PL) spectra (see as examples, **Figure S4**, **Figure 6** and **Figure S5**). Polished z-cut quartz substrates (15 × 15 × 0.5 mm) were purchased from University Wafer.

Preparation for film casting Quartz substrates were cleaned via ultrasonication in isopropyl alcohol for 10 min and exposed to oxygen plasma at ≈ 300 mTorr for 10 min. All subsequent solution preparation and film fabrications were performed in a nitrogen-filled glove box. Precursor solutions for films were fabricated by dissolving EABr, $PbBr_2$ and either FABr or MABr in DMF to make an 0.5 mM solution (based on Pb), in the molar ratio $(EA_{1-x}S_x)_{4.5}Pb_3Br_{10}$, or $MAPbBr_3$ or $FAPbBr_3$ for certain extra characterizations. A slight cation excess was found to be necessary in previous work to form the n = 3 phase, likely due to strong complexation of Pb and Br in DMF. [87] The small excess organic cation likely leaves the film either during spin-casting (most solvent escapes off the film) or during annealing (EA is likely more volatile than MA, as according to Sigma Aldrich, the melting point of ethylammonium chloride is 380-381 K while that of methylammonium chloride is much higher, at 501-506 K). The solutions were left stirring overnight at 3330 K to ensure good dissolution.

Film casting Films were spin-cast at 4000 rpm for 60 seconds without antisolvent rinse, and promptly annealed at 373 K (verified by thermocouple) on a hot plate with a heat diffuser. All spin-cast films were annealed. Some films were drop-cast, whereby a few microliters of the precursor solution was dropped on the substrate, and left for an hour, at which point the film visually appeared solid. Some drop-cast films were annealed. For some experiments (XRD, PL, GIWAXS), after the films cooled, 60 µL of a PMMA solution (75 mg PMMA/3mL toluene) was spin-cast on top of the films at 2000 rpm for 30 seconds. For SEM, PDS, NMR, and FTIR, the same casting procedures were employed, but PMMA was not cast on the films. Films for PDS were cast on separate amorphous quartz substates. Films for FTIR were spin-cast on thin glass slides, so that the Si-O signal wouldn't overwhelm the film signals (the quartz substrates were much thicker). The films were stored in a nitrogen glove box until characterization.

Growth of (EA,FA)$_4$Pb$_3$Br$_{10}$ bulk crystals/powders (EA,FA)$_4$Pb$_3$Br$_{10}$ crystals were grown similarly to the previously-published procedure. [15] Briefly, PbO, EABr and FABr in (EA$_{1-x}$FA$_x$)$_4$Pb$_3$Br$_{10}$ molar ratio were dissolved in HBr, and the solution was heated. Large crystals were formed upon cooling. Individual crystals, "single crystals", were extracted for single-crystal X-Ray analysis. Bulk crystals were drop-cast onto quartz substrates for PL measurements. The bulk crystals were not ground; "powders from bulk crystals" is used to mean that many bulk crystals were dropped onto a substrate and considered a powder. For Figure S2, bulk crystals of (EA)$_4$Pb$_3$Br$_{10}$ were exfoliated onto quartz substrates using scotch tape, following prior work. [12,52]

Powder X-Ray Diffraction (XRD) patterns were obtained using a Panalytical Empyrean powder diffractometer in reflection mode with a Cu-Kα source, operating with an accelerating voltage of 45 kV and beam current of 40 mA. Au nanoparticles (100 nm) drop-cast on quartz substrates were used to calibrate peak positions.

Simulating crystal structures and X-Ray patterns VESTA software [88] was used to plot the crystal structure of (EA)$_4$Pb$_3$Br$_{10}$ (**Figure 1a**), using the CIF determined in prior work. [15] Color schemes for the octahedra and ions were modified, to highlight patterns in octahedral distortions. Bond lengths and angles were also measured using VESTA. Simulated powder XRD patterns were also made using VESTA, from this CIF. [15] For FAPbBr$_3$, a different CIF was used. [71] Simulated GIWAXS patterns were made using this CIF [15] and Python.

GIWAXS characterization. Grazing Incidence Wide-Angle X-Ray Scattering (GIWAXS) experiments were performed on beamline 11-3 (12.7 keV, wiggler side-station) at the Stanford Synchrotron Radiation Lightsource (SSRL). The source-to-detector (two-dimensional Rayonix MX225 CCD) distances were calibrated using lanthanum hexaboride (LaB6). All raw images were geometrically corrected using Nika. Au nanoparticles (100 nm) drop-cast on quartz substrates were used to verify chi-q alignment post-processing. An incidence angle of 0.5° was chosen for the following reasons: (1) it is shallow enough to properly detect the nIP (0k0) peaks (these were cut off when large incidence angles, such as 2°, were used) and (2) it is well above the critical angle. The critical angle was calculated to be near 0.17° using GIXA; [89] this value is slightly below the measured critical angles (0.2°-0.26°) of the BA-MA RP film series. [40] It is important to be far enough above the critical angle to avoid double diffraction, which may manifest in q_Z but not q_{XY}. [90]

Single crystal XRD and refinements. Individual crystals of x_{FA} = 0.09 and 0.17 (the bulk crystals precipitated from acid) were isolated for single crystal XRD analysis. Patterns were collected on a Bruker KAPPA APEX II diffractometer with an APEX II CCD detector, Mo-Kα radiation source (λ = 0.71073 A), and TRIUMPH monochromator. Structures were solved by direct methods and refined by full-matrix least squares on F2 using the OLEX2 program package. Refinements reveal that x_{FA} = 0.09 and 0.17 crystals have an *n* = 3 Ruddlesden-Popper structure in the space group 68, Ccca, which differs from $(EA)_4Pb_3Br_{10}$ (*n* = 3 RP phase in space group 41, C2cb). In addition, **the long axis (b) shrinks with increasing FA**, consistent with more incorporation of the smaller FA cation (see **Table S1**). However, much disorder was observed in the location of Br, possibly due to disorder in the location of FA (see main text). This disorder is reflected in the large R-values obtained (0.2114 ≤ R ≤ 0.3527), which are larger than those obtained in prior work [15] for $(EA)_4Pb_3Br_{10}$ (0.1496 ≤ R ≤ 0.1854).

PDS. Photothermal Deflection Spectroscopy (PDS) measurements were performed using a homebuilt instrument as previously described. [91] Briefly, monochromated light from either a 150 W Xenon or a 100 W halogen lamp is modulated at 0.5 Hz with a mechanical chopper and then split to be separately focused onto the sample and a pyroelectric detector. Degassed and filtered perfluorohexane (C6F14, 3M Fluorinert FC-72) is employed as the deflection medium. The deflection of a HeNe laser aligned perpendicularly to the pump beam to also be parallel and proximal to the sample surface is measured by a position-sensitive Si detector using a lock-in amplifier. Analysis and fitting were performed using MATLAB.). Absorbance peak positions are best determined from UV-Vis (**Figure S5b**), since the PDS signal is less accurate above 3 eV.

Scanning Electron Microscopy was performed using an FEI Nova Nano 650 FEG SEM operating at 7-10 keV accelerating voltage with beam currents of 0.40-0.80 nA. For SEM measurements, the samples were sputter-coated with gold to prevent charging.

Absorbance spectra were extracted from transmission measurements made on a Shimadzu UV-2600 ultraviolet-visible spectrophotometer at room temperature and in ambient conditions.

Photoluminescence (PL) spectra were acquired using a Horiba FluoroMax 4 spectrometer calibrated with Milli-Q water. Photoluminescence spectra reported in in the main text were all collected using an angle of 75° between the excitation and emission port to reduce scattering. Some PL spectra in the

SI were acquired using an angle of 25° for comparison, since the proportions of different features can be angle dependent. All measurements were performed at room temperature (293 K), with an excitation wavelength of 315 nm (3.95 eV). A 345 nm long-pass filter was placed in front of the mission port to reduce scattering. A long-pass filter was always used, when measuring emission. For the measurement in **Figure S2**, an excitation wavelength of 370 nm and long-pass filter of 400 nm were used. An explanation of why scattering is observed more in some samples than others can be found below **Figure S3**. All materials were photostable enough that multiple subsequent scans could be taken without the material changing.

1H-NMR spectra were acquired using a Varian 600 MHz SB VNMRS NMR spectrometer for solutions. Drop-cast and annealed films were scraped off their quartz substrates using a razor blade, and the resulting solutions were dissolved in deuterated DMSO. XRD of drop-cast films confirmed a lack of non-n = 3 phases (**Figure S7**). This procedure was performed in air. Several scan times were employed: 20-minute scans were performed using a 30° pulse and 5 second recycle delay, following previous work. [31] Scans with length varying between 20 minutes and 16h were performed using a 90° pulse and 12 second recycle delay, as described previously. [73] All spectra were referenced to the residual solvent peak for DMSO at 2.50 ppm, and all processing and analysis was done using the TopSpin software package. NMR assignment were made following prior work, [73] as well as from the standard spectrum of DMF from the Chemical Book database. [92]

FTIR spectra were obtained using a Perkin-Elmer Spectrum Two spectrometer equipped with a DTGS detector and diamond windows in the range of 4000-450 cm^{-1} at a resolution of 4 cm^{-1}, or in the range of 3500-1200 cm^{-1} at a resolution of 0.5 cm^{-1}, and in transmission mode.

Supporting Information

Supporting Information is available from the Wiley Online Library or from the author.

Acknowledgements

The authors gratefully acknowledge Dr. Guang Wu of UCSB for single crystal XRD measurements, Dr. Alexander Mikhailovsky and Sepanta Assadi for additional optical measurements, and Dr. Naveen Venkatesan for assistance with simulation of GIWAXS patterns. Growth and structural characterization were supported by the U.S. Department of Energy, Office of Science, Basic Energy Sciences, under Award Number DE-SC-0012541. Support of optical characterization was provided by Quantum Materials for Energy Efficient Neuromorphic Computing, an Energy Frontier Research Center funded by the U.S. Department of Energy (DOE), Office of Science, Basic Energy Sciences, (BES), under Award Number DE-SC0019273. Time-resolved spectroscopy capabilities were supported by DURIP ARO grant 66886LSRIP. Use of the Stanford Synchrotron Radiation Lightsource, SLAC National Accelerator Laboratory, is supported by the U.S. Department of Energy, Office of Science, Office of Basic Energy Sciences under Contract No. DE-AC02-76SF00515. The research reported here also made use the shared facilities of the UCSB MRSEC (National Science Foundation DMR 1720256), a member of the Materials Research Facilities Network (www.mrfn.org). R.M.K. gratefully acknowledges the National Defense Science and Engineering Graduate fellowship for financial support, E.E.M. gratefully acknowledges the NSF Graduate Research Fellowship Program under award number 2139319, and J.R.A.K gratefully acknowledges the National Science Foundation Graduate Research Fellowship under Grant No. 1650114. S.P. gratefully acknowledges support from the Ryan Fellowship and the NSF Graduate Research Fellowship Program under Grant No. DGE-1842165.

Keywords: 2D halide perovskite, emission, solvent, films, crystals, exciton-phonon coupling, self-trapped excitons

Received: ((will be filled in by the editorial staff))
Revised: ((will be filled in by the editorial staff))
Published online: ((will be filled in by the editorial staff))

Conflict of Interest

The authors declare no conflict of interest.

ORCID numbers

Rhiannon M. Kennard, 0000-0003-1181-5638

Clayton J. Dahlman, 0000-0002-4555-4846

Emily E. Morgan, 0000-0002-4992-8243

Joseph R. A. Kincaid, 0000-0003-4976-7432

Yahya Mohtashami, 0000-0003-0121-9998

Shobhana Panuganti, 0000-0003-1762-527X

Richard Schaller, 0000-0001-9696-8830

Ram Seshadri, 0000-0001-5858-4027

Michael Chabinyc, 0000-0003-4641-3508

References

[1] Y. Zhou, J. Chen, O. M. Bakr, O. F. Mohammed, *ACS Energy Lett.* **2021**, *6*, 739.

[2] B. Saparov, D. B. Mitzi, *Chem. Rev.* **2016**, *116*, 4558.

[3] X. Li, J. M. Hoffman, M. G. Kanatzidis, *Chem. Rev.* **2021**.

[4] M. D. Smith, E. J. Crace, A. Jaffe, H. I. Karunadasa, *Annu. Rev. Mater. Res.* **2018**, *48*, 111.

[5] S. N. Ruddlesden, P. Popper, *Acta Crystallogr.* **1958**, *11*, 54.

[6] S. N. Ruddlesden, P. Popper, *Acta Crystallogr.* **1957**, *10*, 538.

[7] I. C. Smith, E. T. Hoke, D. Solis-Ibarra, M. D. McGehee, H. I. Karunadasa, *Angew. Chemie* **2014**, *126*, 11414.

[8] C. C. Stoumpos, D. H. Cao, D. J. Clark, J. Young, J. M. Rondinelli, J. I. Jang, J. T. Hupp, M. G. Kanatzidis, *Chem. Mater.* **2016**, *28*, 2852.

[9] L. Mao, C. C. Stoumpos, M. G. Kanatzidis, *J. Am. Chem. Soc.* **2019**, *141*, 1171.

[10] J. C. Blancon, A. V. Stier, H. Tsai, W. Nie, C. C. Stoumpos, B. Traoré, L. Pedesseau, M. Kepenekian, F. Katsutani, G. T. Noe, J. Kono, S. Tretiak, S. A. Crooker, C. Katan, M. G. Kanatzidis, J. J. Crochet, J. Even, A. D. Mohite, *Nat. Commun.* **2018**, *9*, 1.

[11] R. F. Moral, J. C. Germino, L. G. Bonato, D. B. Almeida, E. M. Therézio, T. D. Z. Atvars, S.

D. Stranks, R. A. Nome, A. F. Nogueira, *Adv. Opt. Mater.* **2020**, *8*, 1.

[12] R. A. Decrescent, X. Du, R. M. Kennard, N. R. Venkatesan, C. J. Dahlman, M. L. Chabinyc, J. A. Schuller, *ACS Nano* **2020**, *14*, 8958.

[13] D. Cortecchia, S. Neutzner, A. R. S. Kandada, E. Mosconi, D. Meggiolaro, F. De Angelis, C. Soci, A. Petrozza, *J. Am. Chem. Soc.* **2017**, *139*, 39.

[14] Z. Ma, F. Li, L. Sui, Y. Shi, R. Fu, K. Yuan, G. Xiao, B. Zou, *Adv. Opt. Mater.* **2020**, *8*, 1.

[15] L. Mao, Y. Wu, C. C. Stoumpos, B. Traore, C. Katan, J. Even, M. R. Wasielewski, M. G. Kanatzidis, *J. Am. Chem. Soc.* **2017**, *139*, 11956.

[16] B. Luo, Y. Guo, X. Li, Y. Xiao, X. Huang, J. Z. Zhang, *J. Phys. Chem. C* **2019**, *123*, 14239.

[17] M. D. Smith, A. Jaffe, E. R. Dohner, A. M. Lindenberg, H. I. Karunadasa, *Chem. Sci.* **2017**, *8*, 4497.

[18] M. D. Smith, B. A. Connor, H. I. Karunadasa, *Chem. Rev.* **2019**, *119*, 3104.

[19] T. Hu, M. D. Smith, E. R. Dohner, M. J. Sher, X. Wu, M. T. Trinh, A. Fisher, J. Corbett, X. Y. Zhu, H. I. Karunadasa, A. M. Lindenberg, *J. Phys. Chem. Lett.* **2016**, *7*, 2258.

[20] E. R. Dohner, E. T. Hoke, H. I. Karunadasa, *J. Am. Chem. Soc.* **2014**, *136*, 1718.

[21] S. Gharibzadeh, I. M. Hossain, P. Fassl, B. A. Nejand, T. Abzieher, M. Schultes, E. Ahlswede, P. Jackson, M. Powalla, S. Schäfer, M. Rienäcker, T. Wietler, R. Peibst, U. Lemmer, B. S. Richards, U. W. Paetzold, *Adv. Funct. Mater.* **2020**, *30*.

[22] S. Gharibzadeh, B. Abdollahi Nejand, M. Jakoby, T. Abzieher, D. Hauschild, S. Moghadamzadeh, J. A. Schwenzer, P. Brenner, R. Schmager, A. A. Haghighirad, L. Weinhardt, U. Lemmer, B. S. Richards, I. A. Howard, U. W. Paetzold, *Adv. Energy Mater.* **2019**, *9*.

[23] A. A. Sutanto, R. Szostak, N. Drigo, V. I. E. Queloz, P. E. Marchezi, J. C. Germino, H. C. N. Tolentino, M. K. Nazeeruddin, A. F. Nogueira, G. Grancini, *Nano Lett.* **2020**, *20*, 3992.

[24] G. Grancini, C. Roldán-Carmona, I. Zimmermann, E. Mosconi, X. Lee, D. Martineau, S. Narbey, F. Oswald, F. De Angelis, M. Graetzel, M. K. Nazeeruddin, *Nat. Commun.* **2017**, *8*, 1.

[25] J. Schlipf, Y. Hu, S. Pratap, L. Bießmann, N. Hohn, L. Porcar, T. Bein, P. Docampo, P. Müller-Buschbaum, *ACS Appl. Energy Mater.* **2019**, *2*, 1011.

[26] N. Yantara, A. Bruno, A. Iqbal, N. F. Jamaludin, C. Soci, S. Mhaisalkar, N. Mathews, *Adv. Mater.* **2018**, *30*, 1.

[27] Z. Xu, Y. Li, X. Liu, C. Ji, H. Chen, L. Li, S. Han, M. Hong, J. Luo, Z. Sun, *Adv. Opt. Mater.* **2019**, *1900308*, 1.

[28] J. Wang, J. Zhang, J. Li, Q. Tan, L. Li, J. Zhang, J. Zang, P. Tan, D. Li, *J. Phys. Chem. Lett.* **2017**, *8*, 6211.

[29] M. Yuan, L. N. Quan, R. Comin, G. Walters, R. Sabatini, O. Voznyy, S. Hoogland, Y. Zhao, E. M. Beauregard, P. Kanjanaboos, Z. Lu, D. H. Kim, E. H. Sargent, *Nat. Nanotechnol.* **2016**, *11*, 872.

[30] C. J. Dahlman, R. A. Decrescent, N. R. Venkatesan, R. M. Kennard, G. Wu, M. A. Everest, J. A. Schuller, M. L. Chabinyc, *Chem. Mater.* **2019**, *31*, 5832.

[31] N. R. Venkatesan, R. M. Kennard, R. A. DeCrescent, H. Nakayama, C. J. Dahlman, E. E. Perry, J. Schuller, M. L. Chabinyc, *Chem. Mater.* **2018**, *30*, 8615.

[32] Y. Chen, J. Hu, Z. Xu, Z. Jiang, S. Chen, B. Xu, X. Xiao, X. Liu, K. Forberich, C. J. Brabec, Y. Mai, F. Guo, *Adv. Funct. Mater.* **2022**, *2112146*, 1.

[33] O. F. Williams, Z. Guo, J. Hu, L. Yan, W. You, A. M. Moran, *J. Chem. Phys.* **2018**, *148*.

[34] M. Zhou, C. Fei, J. S. Sarmiento, H. Wang, *Sol. RRL* **2019**, *3*, 1.

[35] W. L. Tan, Y. B. Cheng, C. R. McNeill, *J. Mater. Chem. A* **2020**, *8*, 12790.

[36] J. C. Blancon, H. Tsai, W. Nie, C. C. Stoumpos, L. Pedesseau, C. Katan, M. Kepenekian, C. M. M. Soe, K. Appavoo, M. Y. Sfeir, S. Tretiak, P. M. Ajayan, M. G. Kanatzidis, J. Even, J. J. Crochet, A. D. Mohite, *Science (80-.).* **2017**, *355*, 1288.

[37] R. Quintero-Bermudez, A. Gold-Parker, A. H. Proppe, R. Munir, Z. Yang, S. O. Kelley, A. Amassian, M. F. Toney, E. H. Sargent, *Nat. Mater.* **2018**, *17*, 900.

[38] J. M. Hoffman, J. Strzalka, N. C. Flanders, I. Hadar, S. A. Cuthriell, Q. Zhang, R. D. Schaller, W. R. Dichtel, L. X. Chen, M. G. Kanatzidis, *Adv. Mater.* **2020**, *32*, 1.

[39] E. Shi, S. Deng, B. Yuan, Y. Gao, Akriti, L. Yuan, C. S. Davis, D. Zemlyanov, Y. Yu, L. Huang, L. Dou, *ACS Nano* **2019**, *13*, 1635.

[40] N. R. Venkatesan, J. G. Labram, M. L. Chabinyc, *ACS Energy Lett.* **2018**, *3*, 380.

[41] K. Liao, C. Li, L. Xie, Y. Yuan, S. Wang, Z. Cao, L. Ding, F. Hao, *Nano-Micro Lett.* **2020**, *12*, 1.

[42] P. Liu, N. Han, W. Wang, R. Ran, W. Zhou, Z. Shao, *Adv. Mater.* **2021**.

[43] L. Yan, J. Hu, Z. Guo, H. Chen, M. F. Toney, A. M. Moran, W. You, *ACS Appl. Mater. Interfaces* **2018**, *10*, 33187.

[44] A. Z. Chen, M. Shiu, X. Deng, M. Mahmoud, D. Zhang, B. J. Foley, S. H. Lee, G. Giri, J. J. Choi, *Chem. Mater.* **2019**, *31*, 1336.

[45] R. Wang, Y. Tong, A. Manzi, K. Wang, Z. Fu, E. Kentzinger, J. Feldmann, A. S. Urban, P. Müller-Buschbaum, H. Frielinghaus, *Adv. Opt. Mater.* **2018**, *6*, 1.

[46] Z. Ren, L. Li, J. Yu, R. Ma, X. Xiao, R. Chen, K. Wang, X. W. Sun, W. J. Yin, W. C. H. Choy, *ACS Energy Lett.* **2020**, *5*, 2569.

[47] P. Mao, J. Zhuang, Y. Wei, N. Chen, Y. Luan, J. Wang, *Sol. RRL* **2019**, *3*, 1.

[48] S. Sidhik, W. Li, M. H. K. Samani, H. Zhang, Y. Wang, J. Hoffman, A. K. Fehr, M. S. Wong, C. Katan, J. Even, A. B. Marciel, M. G. Kanatzidis, J. C. Blancon, A. D. Mohite, *Adv. Mater.* **2021**, *33*, 1.

[49] Y. Shang, Y. Liao, Q. Wei, Z. Wang, B. Xiang, Y. Ke, W. Liu, Z. Ning, *Sci. Adv.* **2019**, *5*.

[50] C. Liang, H. Gu, Y. Xia, Z. Wang, X. Liu, J. Xia, S. Zuo, Y. Hu, X. Gao, W. Hui, L. Chao, T. Niu, M. Fang, H. Lu, H. Dong, H. Yu, S. Chen, X. Ran, L. Song, B. Li, J. Zhang, Y. Peng, G. Shao, J. Wang, Y. Chen, G. Xing, W. Huang, *Nat. Energy* **2020**.

[51] S. Q. Luo, J. F. Wang, B. Yang, Y. B. Yuan, *Front. Phys.* **2019**, *14*.

[52] R. M. Kennard, C. J. Dahlman, J. Chung, B. L. Cotts, A. A. Mikhailovsky, L. Mao, R. A. DeCrescent, K. H. Stone, N. R. Venkatesan, Y. Mohtashami, S. Assadi, A. Salleo, J. A. Schuller, R. Seshadri, M. L. Chabinyc, *Chem. Mater.* **2021**, *33*, 7290.

[53] T. Li, A. M. Zeidell, G. Findik, W. A. Dunlap-Shohl, J. Euvrard, K. Gundogdu, O. D. Jurchescu, D. B. Mitzi, *Chem. Mater.* **2019**, *31*, 4267.

[54] Y. Han, S. Park, C. Kim, M. Lee, I. Hwang, *Nanoscale* **2019**, *11*, 3546.

[55] S. Wang, Y. Yao, J. Kong, S. Zhao, Z. Sun, Z. Wu, L. Li, J. Luo, *Chem. Commun.* **2018**, *54*, 4053.

[56] R. A. DeCrescent, N. R. Venkatesan, C. J. Dahlman, R. M. Kennard, X. Zhang, W. Li, X. Du, M. L. Chabinyc, R. Zia, J. A. Schuller, *Sci. Adv.* **2020**, 1.

[57] D. Cortecchia, J. Yin, A. Bruno, S. Z. A. Lo, G. G. Gurzadyan, S. Mhaisalkar, J. L. Brédas, C. Soci, *J. Mater. Chem. C* **2017**, *5*, 2771.

[58] W. Paritmongkol, E. R. Powers, N. S. Dahod, W. A. Tisdale, *J. Phys. Chem. Lett.* **2020**, *11*, 8565.

[59] J. Yu, J. Kong, W. Hao, X. Guo, H. He, W. R. Leow, Z. Liu, P. Cai, G. Qian, S. Li, X. Chen, X. Chen, *Adv. Mater.* **2019**, *31*, 1.

[60] S. Kahmann, H. Duim, H. H. Fang, M. Dyksik, S. Adjokatse, M. Rivera Medina, M. Pitaro, P. Plochocka, M. A. Loi, *Adv. Funct. Mater.* **2021**, *31*.

[61] S. Li, J. Luo, J. Liu, J. Tang, *J. Phys. Chem. Lett.* **2019**, *10*, 1999.

[62] J. Li, H. Wang, D. Li, *Front. Optoelectron.* **2020**, *13*, 225.

[63] T. Sheikh, A. Shinde, S. Mahamuni, A. Nag, *ACS Energy Lett.* **2018**, *3*, 2940.

[64] J. Li, J. Ma, X. Cheng, Z. Liu, Y. Chen, D. Li, *ACS Nano* **2020**, *14*, 2156.

[65] S. Kahmann, H. Duim, A. J. Rommens, E. K. Tekelenburg, S. Shao, M. A. Loi, *Adv. Opt. Mater.* **2021**, *9*.

[66] G. Kieslich, S. Sun, A. K. Cheetham, *Chem. Sci.* **2015**, *6*, 3430.

[67] M. Becker, T. Klüner, M. Wark, *Dalt. Trans.* **2017**, *46*, 3500.

[68] Y. Fu, M. P. Hautzinger, Z. Luo, F. Wang, D. Pan, M. M. Aristov, I. A. Guzei, A. Pan, X. Zhu, S. Jin, *ACS Cent. Sci.* **2019**, *5*, 1377.

[69] Y. Fu, X. Jiang, X. Li, B. Traore, I. Spanopoulos, C. Katan, J. Even, M. G. Kanatzidis, E. Harel, *J. Am. Chem. Soc.* **2020**, *142*, 4008.

[70] S. Ramos-Terrón, C. Verdugo-Escamilla, L. Camacho, G. de Miguel, *Adv. Opt. Mater.* **2021**, *2*, 1.

[71] I. Spanopoulos, I. Hadar, W. Ke, P. Guo, E. M. Mozur, E. Morgan, S. Wang, D. Zheng, S. Padgaonkar, G. N. M. Reddy, E. A. Weiss, M. C. Hersam, R. Seshadri, R. D. Schaller, M. G. Kanatzidis, **2021**.

[72] S. A. Fateev, A. A. Petrov, E. I. Marchenko, Y. V. Zubavichus, V. N. Khrustalev, A. V. Petrov, S. M. Aksenov, E. A. Goodilin, A. B. Tarasov, *Chem. Mater.* **2021**, *33*, 1900.

[73] W. T. M. Van Gompel, R. Herckens, G. Reekmans, B. Ruttens, J. D'Haen, P. Adriaensens, L. Lutsen, D. Vanderzande, *J. Phys. Chem. C* **2018**, *122*, 4117.

[74] Q. Li, Z. Chen, M. Li, B. Xu, J. Han, Z. Luo, L. Tan, Z. Xia, Z. Quan, *Angew. Chemie - Int. Ed.* **2021**, *60*, 2583.

[75] E. Benassi, H. Fan, *J. Mol. Liq.* **2020**, *313*, 113202.

[76] D. B. Mitzi, D. R. Medeiros, P. R. L. Malenfant, I. B. M. T. J. Watson, P. O. Box, Y. Heights, N. York, **2002**, *41*, 2134.

[77] M. Shin, J. Kim, Y. K. Jung, T. petri Ruoko, A. Priimagi, A. Walsh, B. Shin, *J. Mater. Chem. C* **2019**, *7*, 3945.

[78] A. A. Petrov, S. A. Fateev, V. N. Khrustalev, Y. Li, P. V. Dorovatovskii, Y. V. Zubavichus,

E. A. Goodilin, A. B. Tarasov, *Chem. Mater.* **2020**, *32*, 7739.

[79] Q. Du, C. Zhu, Z. Yin, G. Na, C. Cheng, Y. Han, N. Liu, X. Niu, H. Zhou, H. Chen, L. Zhang, S. Jin, Q. Chen, *ACS Nano* **2020**, *14*, 5806.

[80] A. A. Koegel, E. M. Mozur, I. W. H. Oswald, N. H. Jalarvo, T. R. Prisk, M. Tyagi, J. R. Neilson, **2021**.

[81] C. J. Dahlman, R. M. Kennard, P. Paluch, N. R. Venkatesan, M. L. Chabinyc, G. N. Manjunatha Reddy, *Chem. Mater.* **2021**, *33*, 642.

[82] K. S. S. R. T. Williams, *J. Phys. Chem. Solids* **1990**, *51*, 679.

[83] Q. Tu, I. Spanopoulos, S. Hao, C. Wolverton, M. G. Kanatzidis, G. S. Shekhawat, V. P. Dravid, *ACS Energy Lett.* **2019**, *4*, 796.

[84] K. A. Bush, N. Rolston, A. Gold-Parker, S. Manzoor, J. Hausele, Z. J. Yu, J. A. Raiford, R. Cheacharoen, Z. C. Holman, M. F. Toney, R. H. Dauskardt, M. D. McGehee, *ACS Energy Lett.* **2018**, *3*, 1225.

[85] S. De Wolf, J. Holovsky, S. J. Moon, P. Löper, B. Niesen, M. Ledinsky, F. J. Haug, J. H. Yum, C. Ballif, *J. Phys. Chem. Lett.* **2014**, *5*, 1035.

[86] M. J. Carnie, C. Charbonneau, M. L. Davies, J. Troughton, T. M. Watson, K. Wojciechowski, H. Snaith, D. A. Worsley, *Chem. Commun.* **2013**, *49*, 7893.

[87] K. et Al, .

[88] K. Momma, F. Izumi, *J. Appl. Crystallogr.* **2011**, *44*, 1272.

[89] GIXA Calculator for Penetration Depth (and Optical Properties) for X-rays, .

[90] R. Resel, M. Bainschab, A. Pichler, T. DIngemans, C. Simbrunner, J. Stangl, I. Salzmann, *J. Synchrotron Radiat.* **2016**, *23*, 729.

[91] K. Vandewal, S. Albrecht, E. T. Hoke, K. R. Graham, J. Widmer, J. D. Douglas, M. Schubert, W. R. Mateker, J. T. Bloking, G. F. Burkhard, A. Sellinger, J. M. J. Fréchet, A. Amassian, M. K. Riede, M. D. McGehee, D. Neher, A. Salleo, *Nat. Mater.* **2014**, *13*, 63.

[92] N,N Dimethylformamide(68-12-2) 1H NMR, **2017**.

Table of Contents

Schematic structure of an $(EA_{1-x}FA_x)_4Pb_3Br_{10}$·DMF film, showing possible locations of formamidinium (FA) and dimethylformamide (DMF). Ethylammonium (EA) cations are not shown for clarity. The right panel shows photoluminescence spectra of $(EA_{1-x}FA_x)_4Pb_3Br_{10}$·DMF and $(EA_4Pb_3Br_{10}$ spin-cast films: the presence of FA-DMF causes the extinction of a phonon-coupled peak.

Rhiannon M. Kennard, Clayton J. Dahlman, Emily E. Morgan, Guang Wu, Juil Chung, Benjamin L. Cotts, Alexander Mikhailovsky, Lingling Mao, Joseph R. A. Kincaid, Ryan A. DeCrescent, Kevin H. Stone, Shobhana Panuganti, Naveen R. Venkatesan, Yahya Mohtashami, Sepanta Assadi, Mercouri G. Kanatzidis, Alberto Salleo, Jon A. Schuller, Ram Seshadri, and Michael L. Chabinyc. *

Enhancing and Extinguishing the Different Emission Features of Two-Dimensional $(EA_{1-x}FA_x)_4Pb_3Br_{10}$ Perovskite Films

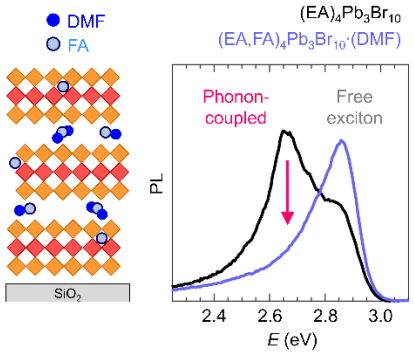

Enhancing and Extinguishing the Different Emission Features of Two-Dimensional $(EA_{1-x}FA_x)_4Pb_3Br_{10}$ Perovskite Films

Supporting Information

*Rhiannon M. Kennard, † Clayton J. Dahlman, † Emily E. Morgan, †∞ Juil Chung, † Benjamin L. Cotts, # Joseph R. A. Kincaid, + Ryan A. DeCrescent, ‡ Kevin H. Stone, ▪ Shobhana Panuganti, ° Yahya Mohtashami, ‖ Lingling Mao, †∞ Richard D. Schaller, °≈ Alberto Salleo, # Mercouri G. Kanatzidis, ° Jon A. Schuller, ‖ Ram Seshadri, †∞+ Michael L. Chabinyc. †**

Rhiannon M. Kennard, Clayton J. Dahlman, Emily E. Morgan, Juil Chung, Lingling Mao, Ram Seshadri, and Michael L. Chabinyc *
† Materials Department, University of California, Santa Barbara, CA 93106, USA
***Email: mchabinyc@engineering.ucsb.edu**

Emily E. Morgan, Lingling Mao, Ram Seshadri
∞ Materials Research Laboratory, University of California, Santa Barbara, CA 93106, USA

Joseph R. A. Kincaid, Ram Seshadri
+Department of Chemistry and Biochemistry, University of California, Santa Barbara, CA 93106, USA

Benjamin L. Cotts, Alberto Salleo
Department of Materials Science and Engineering, Stanford University, 496 Lomita Mall, Suite 102 Stanford, CA 94305, USA

Ryan A. DeCrescent
‡ Department of Physics, University of California, Santa Barbara, CA 93106, USA

Kevin H. Stone
▪ SSRL, SLAC National Accelerator Laboratory, Menlo Park, CA 94025, USA.

Shobhana Panuganti, Mercouri G. Kanatzidis, Richard D. Schaller
° Department of Chemistry, Northwestern University, Evanston, IL 60208, USA

≈ Richard D. Schaller
Center for Nanoscale Materials, Argonne National Laboratory, Lemont, IL 60439, USA

Yahya Mohtashami, Jon A. Schuller
‖ Department of Electrical and Computer Engineering, University of California, Santa Barbara, CA 93106, USA

Table of Contents

Table S1. Unit cells of x_{FA} = 0.09 and 0.17 crystals precipitated from aqueous HBr, with reported unit cell of $(EA)_4Pb_3Br_{10}$ for comparison. [1] The b-axis (perpendicular to the 2D sheets) is in bold blue to highlight the contraction with increasing FA. Full refinements were unsuccessful due to disorder in the location of Br (possibly caused by disorder in the location of FA, as discussed in the main text), but unit cell dimensions were extracted and are reported below:

Crystal	**$(EA)_4Pb_3Br_{10}$ (from [1])**	**x_{FA} = 0.09**	**x_{FA} = 0.17**
Temperature	293 K	296(2) K	293(2) K
Wavelength	0.71073 Å	0.71073 Å	0.71073 Å
Crystal system	Orthorhombic	Orthorhombic	Orthorhombic
Space group	C2cb	Ccca	Ccca
Unit cell dimensions	a = 8.4267(12) Å, α = 90° **b = 46.351(5) Å**, β = 90° c = 8.4298(10) Å, γ = 90°	a = 8.4199(11) Å α = 90° **b = 46.305(6) Å** β = 90° c = 8.4216(10) Å γ = 90°	a = 8.4356 (12) Å α = 90° **b = 46.240 (6) Å** β = 90° c = 8.4282 (12) Å γ = 90°

Section S2: Fitting the PDS Data

Following previous work, [2–4] the Urbach tails were fit according to:

$$PDS = A\ exp\left(\frac{E - E_G}{E_U}\right)$$

Where PDS is the PDS signal from **Figure 7**, where A is a prefactor, E_G is the bandgap and E_U is the Urbach energy.

The goodness of fits are as follows (from MATLAB):

$(EA)_4Pb_3Br_{10}$ spin-cast film; E_U = 54 meV
sse: 942.3958e-006
rsquare: 997.5532e-003
dfe: 29.0000e+000
adjrsquare: 997.3844e-003
rmse: 5.7006e-003

$(EA)_4Pb_3Br_{10}$ spin-cast film; E_U = 45 meV
sse: 21.1291e-006
rsquare: 998.2440e-003
dfe: 60.0000e+000
adjrsquare: 998.1855e-003
rmse: 593.4233e-006

X_{FA} = 0.07 spin-cast film
sse: 1.3240e-003
rsquare: 998.2726e-003
dfe: 78.0000e+000
adjrsquare: 998.2283e-003
rmse: 4.1200e-003

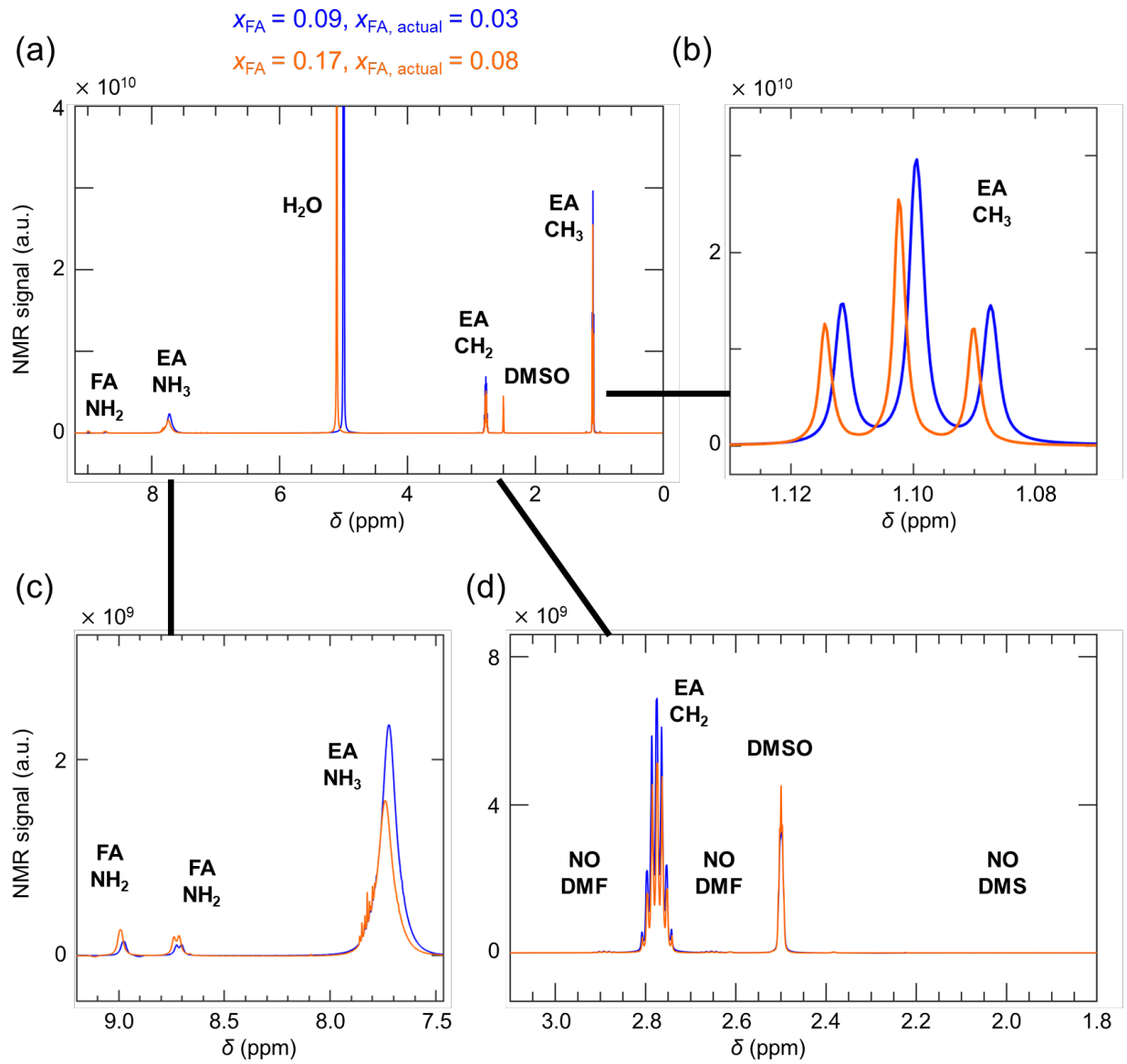

Figure S1. Proton NMR of bulk crystals with $(EA_{1-x}FA_x)_4Pb_3Br_{10}$ stoichiometry grown from $(HBr)_{aq}$, dissolved in deuterated DMSO-d6. The compositions refer to the stoichiometric amount of FA relative to EA *in the precursor solution,* $x_{FA,}$ and the resulting solid has approximately $(EA_{1-x}FA_x)_4Pb_3Br_{10}$ stoichiometry. The *actual* amount of FA in the $(EA_{1-x}FA_x)_4Pb_3Br_{10}$ stoichiometry is verified by NMR, and is designated $x_{FA,\ actual}$. (a) shows the full spectra, (b), (c) and (d) show specific regions of interest.

NMR assignments were made following prior work. [5] NMR confirms the presence of both EA and FA in the bulk crystals. The proportion of EA: FA was calculated by integrating the peaks and using the expression:

$$\frac{Moles\ EA}{Moles\ FA} = \frac{Integration\ for\ EA}{Integration\ for\ FA} \times \frac{Number\ of\ H\ in\ FA\ signal}{Number\ of\ H\ in\ EA\ signal}$$

The *actual* amount of FA, $x_{FA,\ actual}$, were about half of the x_{FA} in the precursor solution, likely due to different complexation of FA and EA in the precursor solution. All peaks correspond to either EA, FA, DMSO or H_2O, and no peaks are unaccounted for. As expected, no DMF is present, as no DMF was used during bulk crystal synthesis. The H_2O peak near 5 ppm is downshifted relative to the H_2O peak in the NMR spectra of films (**Figure S8**). This might be due to a small amount of $(HBr)_{aq}$ leftover from the synthesis. If $(HBr)_{aq}$ were present, we would expect a reaction with DMSO to yield dimethyl sulfide (DMS), which has a peak near 2 ppm. There is no DMS peak near 2 ppm, so either 1) the $(HBr)_{aq}$ stayed in pockets of water and did not react with the DMSO, or 2) the amount of residual $(HBr)_{aq}$ in the bulk crystals is negligible. In any case, the possible presence of residual $(HBr)_{aq}$ has negligible impact on the optical properties: $(EA)_4Pb_3Br_{10}$ bulk crystals grown from $(HBr)_{aq}$ and $(EA)_4Pb_3Br_{10}$ drop-cast films made from DMF all have the free exciton, Ph-1 and Ph-2 in the same proportions, as previously published. [4]

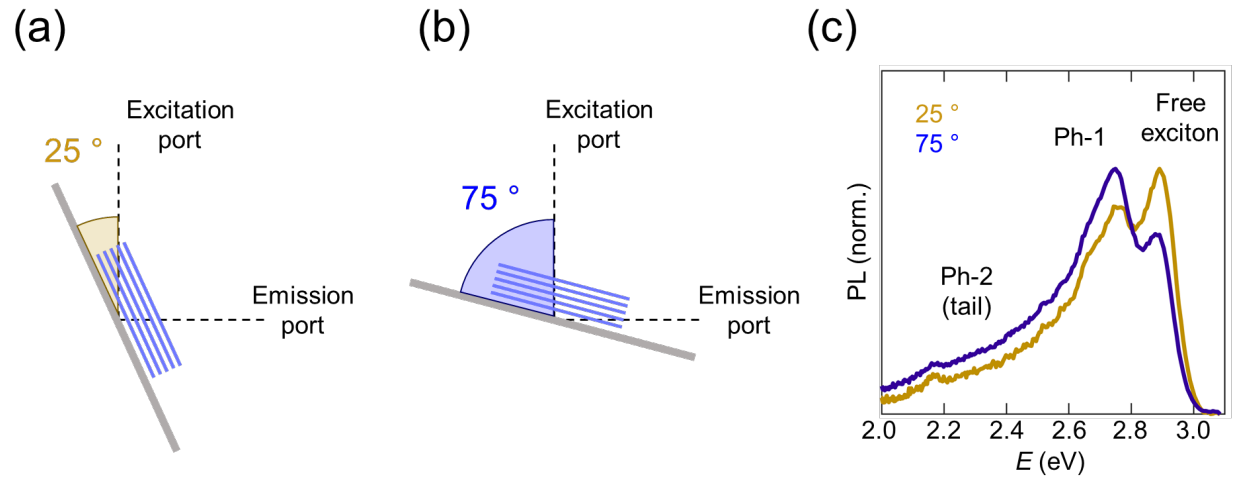

Figure S2. PL emission of exfoliated flakes of $(EA)_4Pb_3Br_{10}$ bulk crystals at different angles. Schematics of the experiment at 25° (a) and 75° (b), with normalized emission spectra (c) taken at 295 K and 3.35 eV excitation (370 nm). For this measurement, a 400 nm long-pass filter was used. The 2D, Pb-Br sheets of $(EA)_4Pb_3Br_{10}$ are represented by blue lines.

Bulk crystals of $(EA)_4Pb_3Br_{10}$ were exfoliated onto substrates using scotch tape, following prior work.[6,7] This was done to ensure that the 2D sheets would be well-aligned, parallel to the substrate.[6,7] The angle of emission was varied by rotating the sample stage with respect to the excitation and emission ports. When the 2D sheets are examined from the front (25°; **Figure S2a**), Ph-1 is weaker. In contrast, when the 2D sheets are examined from the side (75°; **Figure S2b**), Ph-1 is stronger. Ph-1 therefore behaves like the self-trapped exciton reported previously, that is p-like and associated with a magnetic dipole transition.[6,8] However, Ph-2 shows no change with angle, so Ph-2 is likely a different type of feature.

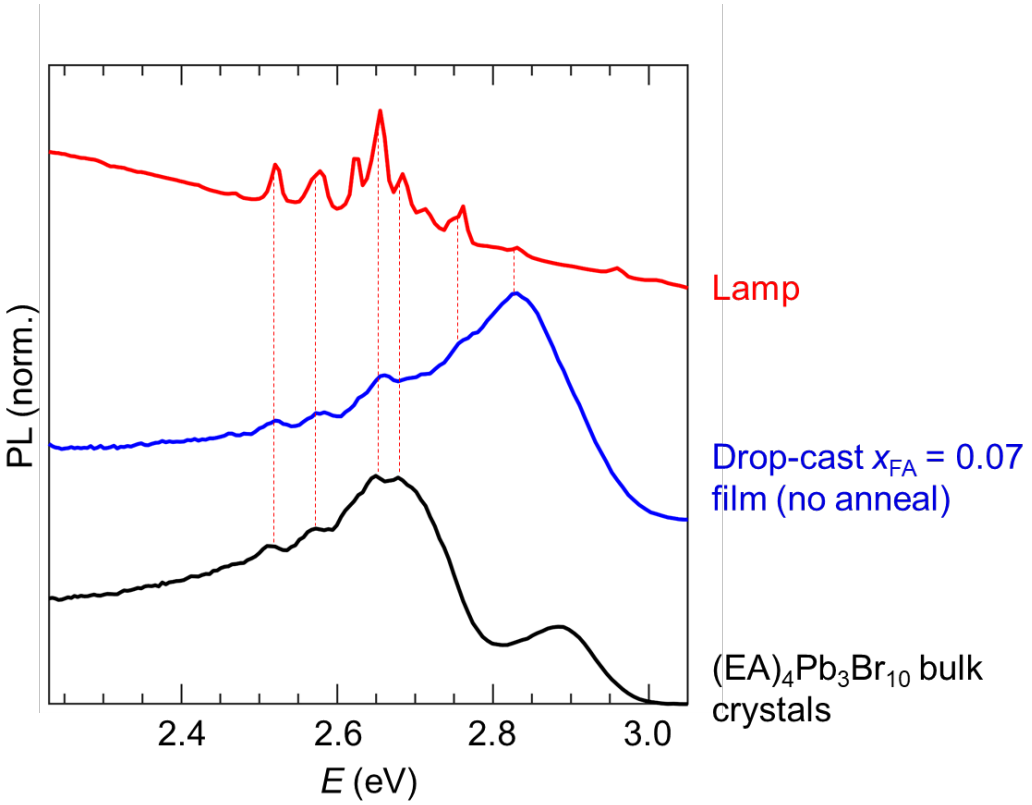

Figure S3. Emission spectrum of the excitation source (lamp) used for photoluminescence experiments, in the 2.3-3 eV region (data taken at 293 K). A monochromator is employed to select 3.95 eV as the excitation energy. However, the lamp itself emits across the visible spectrum, and has several sharp peaks near 2.6 eV. Incomplete filtering of these peaks by the monochromator results in these peaks appearing in the spectra of the samples studied here. Two samples are shown (discussed elsewhere), with different composition; both contain weak lamp peaks.

A long-pass filter was used for all measurements on the fluorimeter, to mitigate the incomplete filtering seen in **Figure S3**. The lamp peaks are particularly noticeable in samples that are not continuous along the quartz substrate: drop-cast films and bulk crystals. This is because the excitation light scatters particularly well off the polished surface of the quartz. For spin-cast films (**Figure 6**), this scattering is much less of a problem, because the perovskite film is continuous across the substrate, so the quartz is less exposed. To verify that the measured intensities of all emission features (free exciton, Ph-1 and Ph-2) are accurate using the fluorimeter, we also measured emission using a laser-based setup that does not have this incomplete filtering problem (see "temperature-dependent photoluminescence" section of prior work [7]). The intensities of the FE, Ph-1 and Ph-2 are the same when using the laser setup and the fluorimeter, for both bulk crystals and drop-cast films, [7] confirming the accuracy of our fluorimeter measurements.

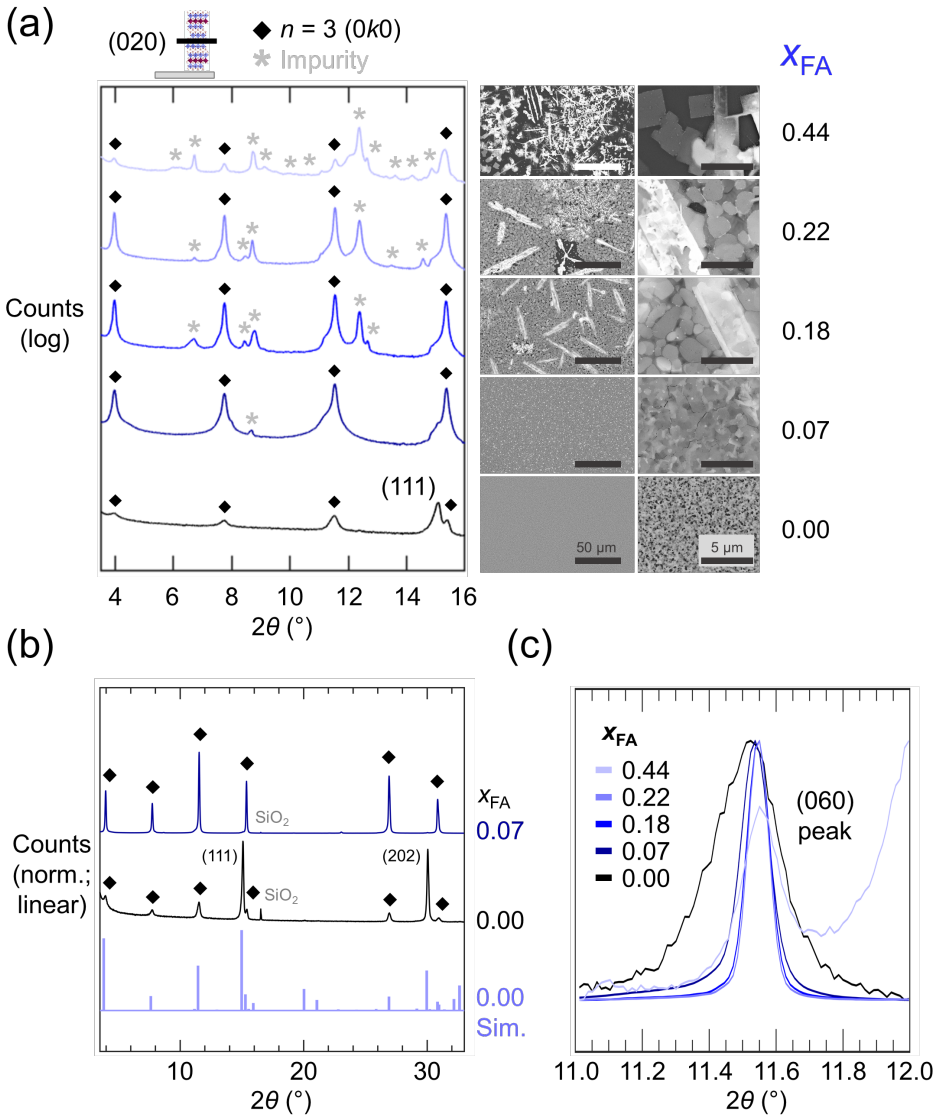

Figure S4. Structural characterization of spin-cast films with different x_{FA}. (a) XRD patterns of films shown on a logarithmic scale, with corresponding SEM images. The n = 3 (0k0) peaks are indicated with diamonds, and the n = 3 (111) peak is also indicated. A schematic of the (020) plane is shown as an example of (0k0). (b) XRD patterns of spin-cast x_{FA} = 0.07 and x_{FA} = 0.00 on a linear scale, compared with the simulated pattern for x_{FA} = 0.00. (0k0) peaks are marked by the black diamonds; (111) and (202) peaks as labelled, and SiO_2 peaks from the substrate labelled as well. (c) Closer examination of the (060) peak.

Spin-cast films with FA substitution exhibit an RP n = 3 structure, with impurities appearing for larger amounts of FA. **Figure S4a** shows the X-Ray Diffraction (XRD) patterns of films with $0.00 \leq x_{FA} \leq 0.44$. The initial (0$k$0) features of $(EA)_4Pb_3Br_{10}$, which are signatures of the n = 3 phase, can be found in all FA-substituted films. [1,9] The (111) peak disappears, signaling a change in crystallite orientation with FA substitution. The FA-substituted films have crystallites oriented out-of-plane, such that the Pb-Br

semiconducting sheets are parallel to the substrate (cartoon in **Figure S4a**). In addition, the XRD peaks increase by an order of magnitude with FA substitution, consistent with larger domain size (**Figure S4a-b**). This increase is especially remarkable because the film thickness is similar after FA substitution (**Figure 5**). In addition, the peak width of the compositions with FA is also considerably narrower, again reflecting larger domain size (**Figure S4c**). Non-n = 3 peaks are clearly visible for most FA loadings, suggesting impurity formation.

To better understand n = 3 and impurity growth, we examined the structure of the films using Scanning Electron Microscopy (SEM). The x_{FA} = 0.07 film appears homogeneous via SEM, consistent with n = 3 being the predominant phase seen in XRD. In contrast, the x_{FA} = 0.18 film exhibits large, needle-like impurities, consistent with impurity peaks readily appearing in XRD. The needle-like shape of the impurities suggests that they are 1-D phases, as the habit of 1D phases in similarly-grown films is needles. [3] More impurities appeared for x_{FA} = 0.22 and x_{FA} = 0.44, with different crystal habit, suggesting impurities of different phases. The obvious presence of these impurities in XRD and SEM contrasts with the behavior of impurities in $(BA)_2(MA)_{n-1}Pb_nI_{3n+1}$ RP films. Impurities in $(BA)_2(MA)_{n-1}Pb_nI_{3n+1}$ RP films are often off-target n RP phases, and they form intergrown into the same grain as the RP of targeted n, [10,11] and as such are indistinguishable in SEM.

No emission was observed from the very small amount of impurity in the x_{FA} = 0.07 films (**Figure S5**). While this impurity may contain DMF, the lattice expansion of the n = 3 phase when more DMF is present (**Figure S7**) confirms that DMF is being incorporated into the n = 3 phase.

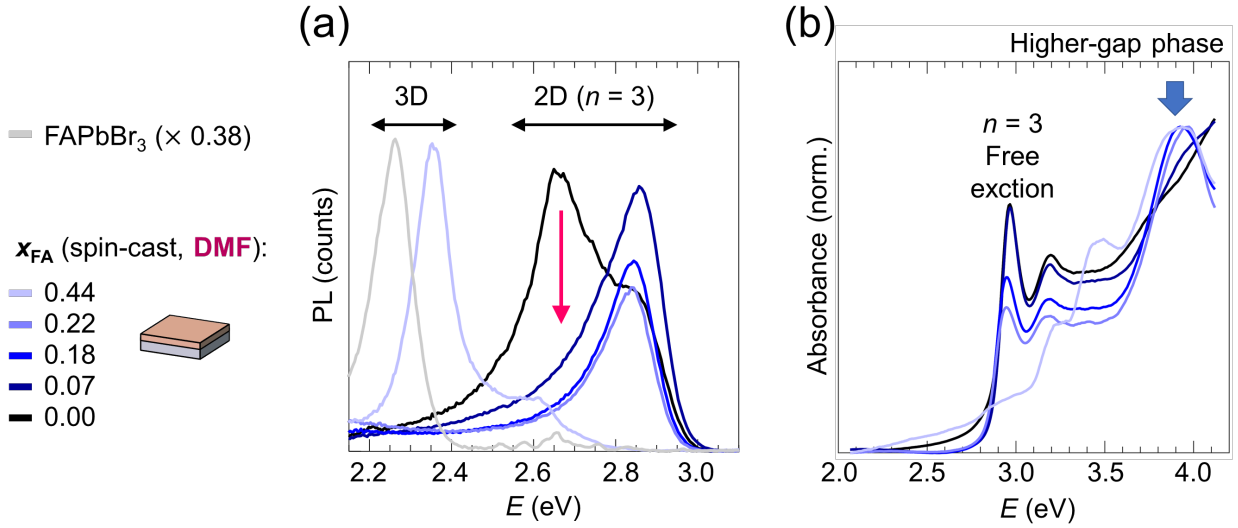

Figure S5. (a) Photoluminescence of spin-cast films with different x_{FA} for 3.94 eV excitation. 2D (n = 3) emission is retained until x_{FA} = 0.22, with x_{FA} = 0.44 having emission from the 3D (EA,FA)$PbBr_3$ phase. The intensity of a $FAPbBr_3$ film, made for comparison, is multiplied by 0.38. (c) UV-Vis absorbance of the x_{FA} films. A higher-gap phase is indicated by the arrow, and likely corresponds to the impurities seen in **Figure S4**.

For most of the FA compositions, the photoluminescence of the spin-cast films is from the n = 3 phase, despite the films containing impurities. **Figure S5a** shows the photoluminescence emission of the films with $0.00 \le x_{FA} \le 0.44$, as well as of an $FAPbBr_3$ film for comparison. Prior work on $(EA)_4Pb_3Br_{10}$ (x_{FA} = 0.00) identified the emission peak at 2.9 eV to be a free exciton (FE), and found that the 2.7 eV peak and the low-energy tail are phonon-coupled. [4] The free exciton emission of the n = 3 phase at 2.9 eV is retained for all $0.00 \le x_{FA} \le 0.22$. Thus, emission coming from the n = 3 phase is retained until very high FA substitution despite obvious non-n = 3 phases appearing in both XRD and SEM (**Figure S4**). This suggests that emission from these non-n = 3 phases is not observed, similarly to how emission from PbI_2 or $PbBr_2$ is not observed in $MAPbX_3$ films. This interpretation is confirmed by UV-Vis absorbance measurements, which reveal a peak near 4 eV that gets stronger with increasing FA content (**Figure S5b**). The absence of emissive impurities contrasts with the behavior of $(BA)_2(MA)_{n-1}Pb_nI_{3n+1}$ RP films, in which off-target n RP phases with smaller bandgap dominate the emission. [3,10–13] The x_{FA} = 0.44 film exhibits emission similar in location and peak shape to $FAPbBr_3$, and has absorbance onset near 2.2 eV (**Figure S5b**) suggesting that the emission from the x_{FA} = 0.44 film comes from the (EA,FA)$PbBr_3$ alloy (see also **Figure S6** [14]). The (EA,FA)$PbBr_3$ alloy has blue-shifted emission from $FAPbBr_3$, likely because EA widens the gap, consistent with prior work showing that the (EA,MA)$PbBr_3$ alloy has larger gap than $MAPbBr_3$. [15] Overall, most films with FA substitution exhibit emission from the n = 3 phase.

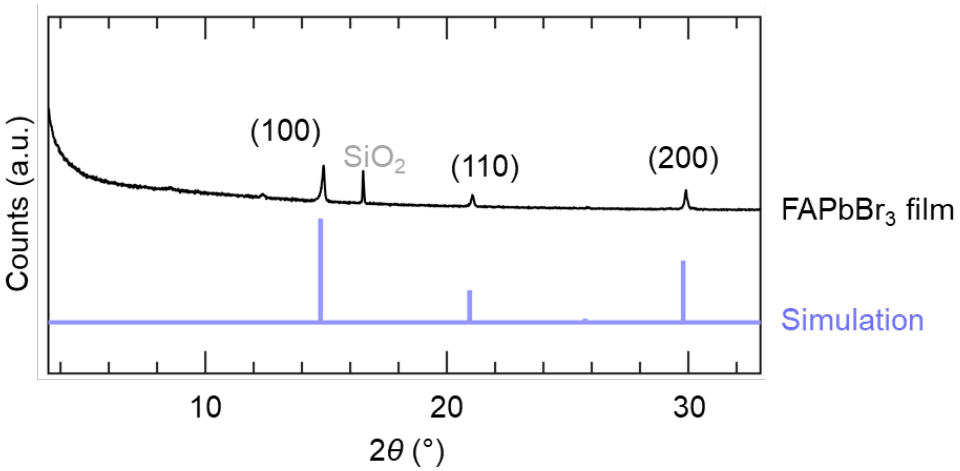

Figure S6. XRD pattern of the spin-cast $FAPbBr_3$ film, with peaks indicated. The pattern was well-matched with the simulation. The 3D cubic phase contains no peaks at low angle.

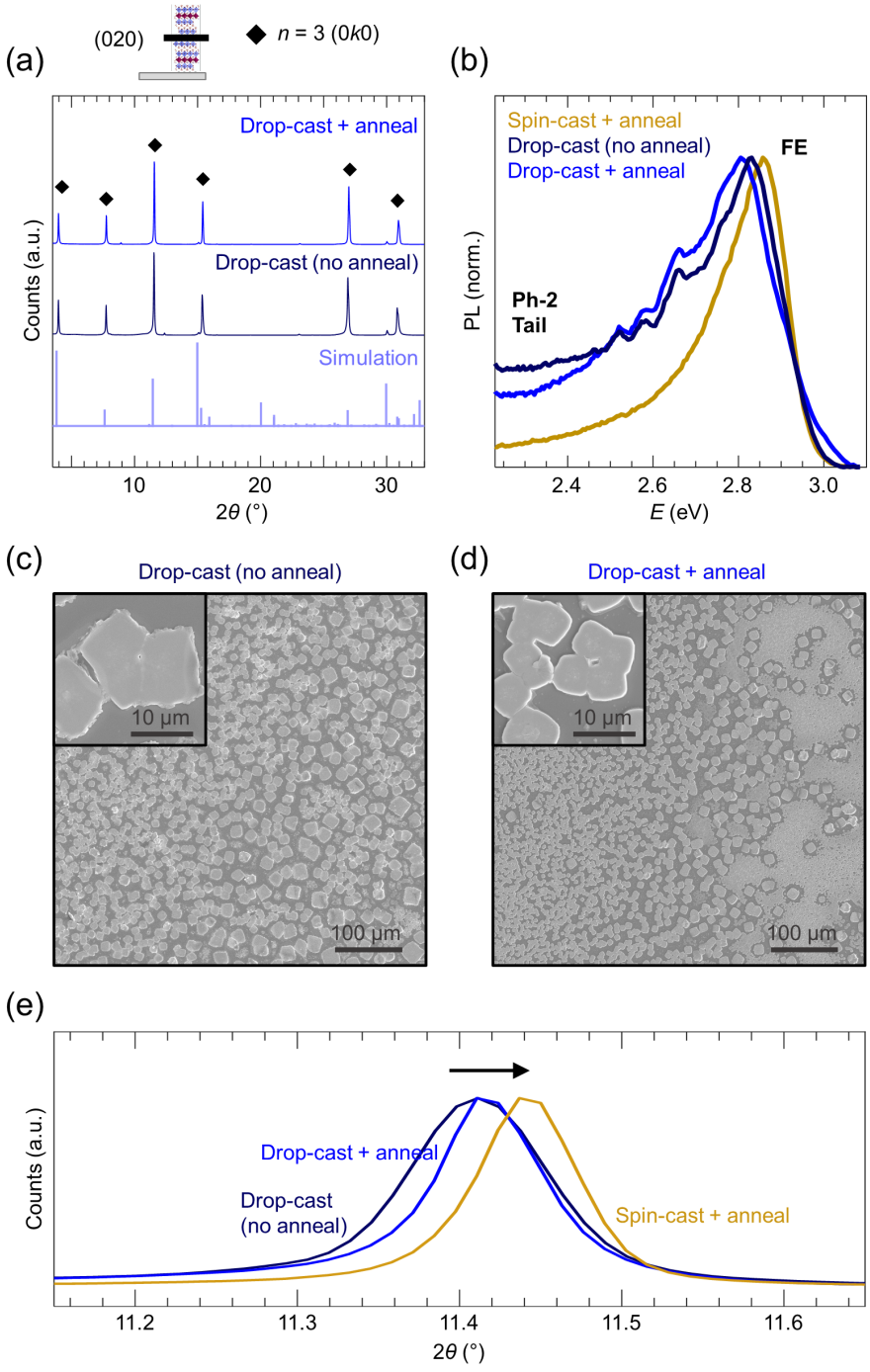

Figure S7. Structural and optical properties of drop-cast films of x_{FA} = 0.07. (a) XRD of drop-cast films, with and without annealing, of x_{FA} = 0.07. The simulated pattern of $(EA)_4Pb_3Br_{10}$ is also shown. (b) PL emission of these films and of the spin-cast film of x_{FA} = 0.07 film, with 3.95 eV excitation and 75 ° collection angle. FE stands for free exciton, and Ph-2 stands for phonon-coupled emission (the 2nd phonon-coupled peak; the 1st one is at 2.7 eV and is not present in x_{FA} films). (c-d) SEM of drop-cast films, with and without annealing. (e) The (060) peak (XRD), showing a lattice contraction when less DMF is in the structure.

The drop-cast films contain primarily the *n* = 3 phase, and are oriented uniformly with the semiconducting sheets parallel to the substrate. The grains are micron-scale, and are unconstrained. SEM confirms that only one crystal habit is present, likely corresponding to an *n* = 3 phase. The phonon-coupled emission tail at low energy (Ph-2) is more pronounced when making the films via drop-casting, than it is using spin-casting. Similar results were found for drop-cast films of $(EA)_4Pb_3Br_{10}$. [4] Notably, the drop-cast films do not have the 2.7 eV emission (Ph-1), despite the low-energy tail being present. This verifies that growth conditions are not responsible for turning off the 2.7 eV peak.

Additionally, the drop-cast films have larger b-axis lattice spacing than the spin-cast film. This is likely because the drop-cast films contain more DMF, as is suggested by the FTIR and NMR data (**Figure S8, S12**). In the drop-cast films, annealing contracts the lattice slightly; perhaps because some DMF is removed upon annealing. Changes to lattice spacing and octahedral distortions [16] with the presence of FA/DMF may explain the slight red-shift in the free exciton.

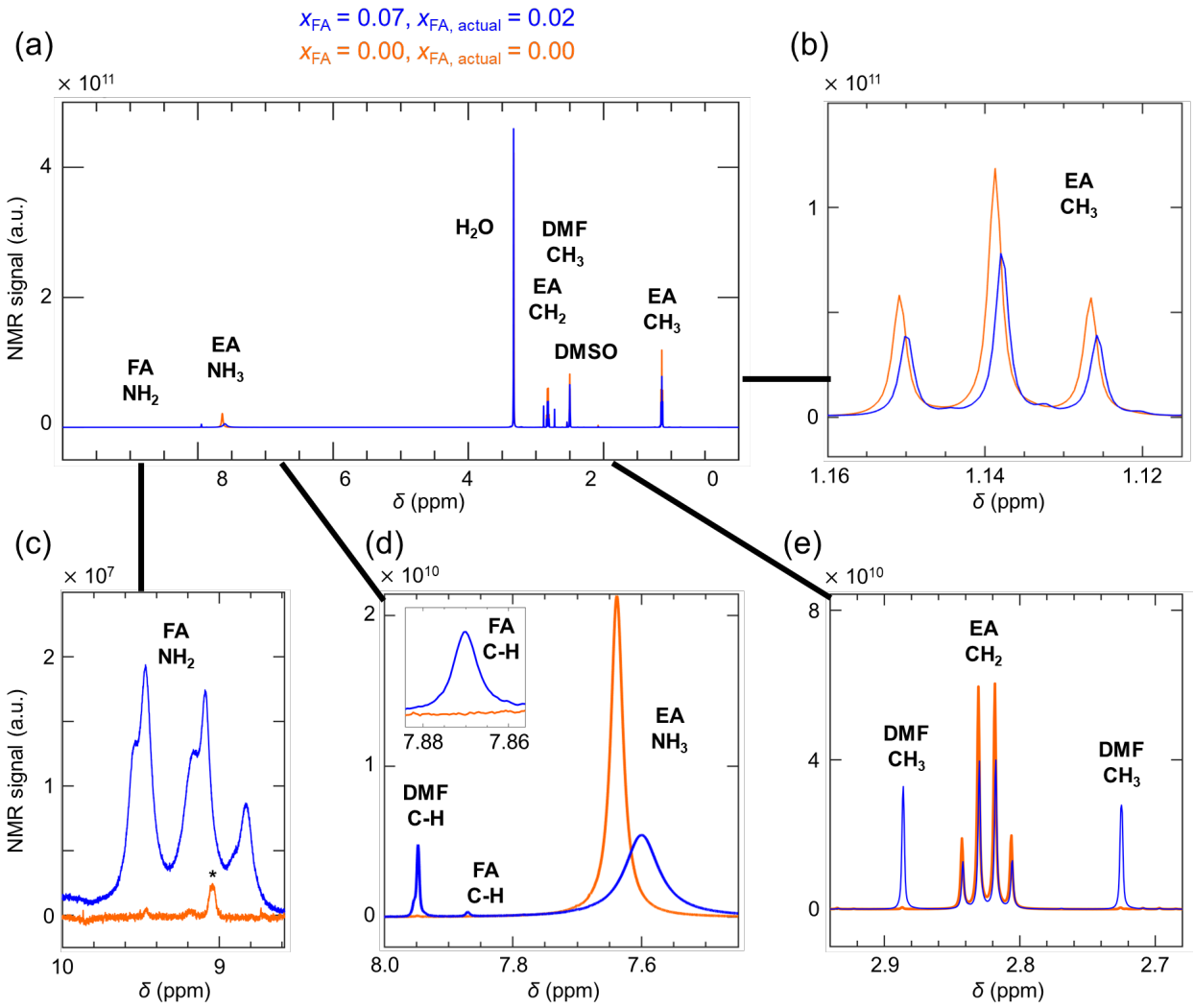

Figure S8. 1H-NMR spectra of drop-cast and annealed films with x_{FA} = 0.07 and x_{FA} = 0.00 compositions prepared from DMF (no PMMA capping layer), that were then scraped off the substrates and dissolved in deuterated DMSO-d6. (a) shows the full spectra, (b), (c), (d) and (e) show specific regions of interest. The * in (c) is explained below.

NMR assignment were made following prior work, [5] as well as from the standard spectrum of DMF from the Chemical Book database. [17] NMR spectra of drop-cast films revealed EA, DMF and a small amount of FA. No extra peaks were observed. No reactions are expected here, as the drop-cast films do not contain $(HBr)_{aq}$. The EA CH_3 and CH_2 peaks are down-shifted for the drop-cast samples compared to for the bulk crystal samples, perhaps due to interactions with DMF for the drop-cast samples.

NMR analysis confirmed that the x_{FA} = 0.07 composition (drop-cast and annealed; see **Figure S7** for XRD) had both FA and DMF. For integration, the EA and DMF peaks near 2.8 ppm were used and the FA peaks near 9 ppm were used, as these had low overlap with other features. Peak integration yielded EA: DMF of 0.998: 0.002 for the x_{FA} = 0.00 sample and EA: DMF: FA of 0.79: 0.19: 0.02 for the x_{FA} = 0.07 sample. FA and EA are approximately in the proportions expected from weighing out the powders; as 0.02 / (0.79 + 0.02) ≈ 0.02, which is not very far off from 0.07 (the difference likely

originates from different complexation of FA and EA in the precursor solution). All relative ratios were obtained using:

$$\frac{Moles\ EA}{Moles\ DMF} = \frac{Integration\ for\ EA}{Integration\ for\ DMF} \times \frac{Number\ of\ H\ in\ DMF\ signal}{Number\ of\ H\ in\ EA\ signal}$$

and

$$\frac{Moles\ EA}{Moles\ FA} = \frac{Integration\ for\ EA}{Integration\ for\ FA} \times \frac{Number\ of\ H\ in\ FA\ signal}{Number\ of\ H\ in\ EA\ signal}$$

The same NMR experiment was tried on spin-cast samples; however, a very large number of samples was required to have sufficient material for the NMR measurement; and the time scale needed to scrape all these samples in air raised concerns of degradation. Thus, FTIR, which is a rapid technique, was preferred for the spin-cast samples.

Regarding the * in panel (c), the EABr precursor used was 98% pure (from Sigma Aldrich), so it is possible that a very small amount of impurity is present. Regardless, the FA-NH_2 peaks are clearly present for the x_{FA} = 0.07 drop-cast film, and clearly absent for the x_{FA} = 0.00 drop-cast film.

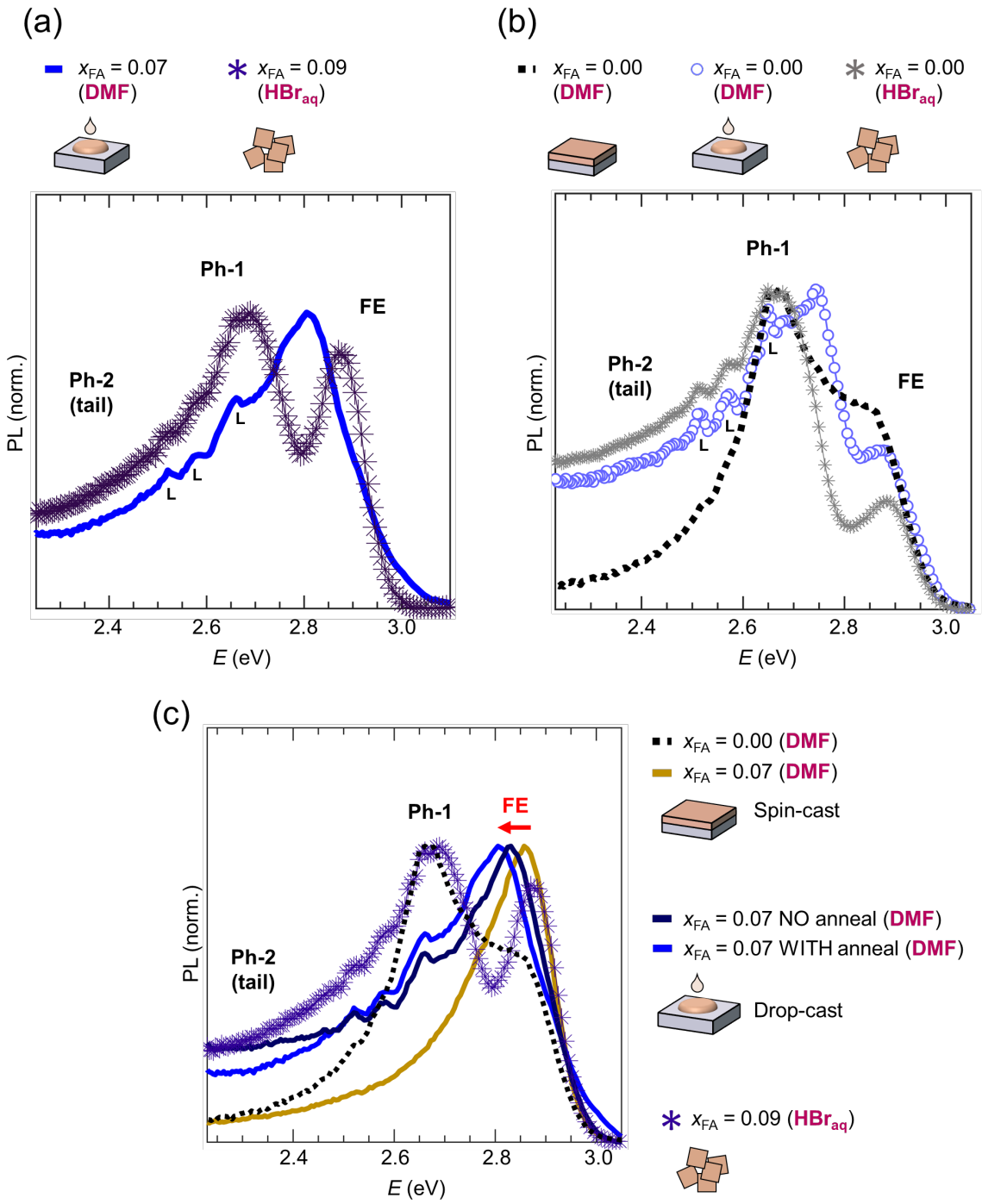

Figure S9. (a) Photoluminescence of bulk crystals (x_{FA} = 0.09, $x_{FA,\ actual}$ = 0.03) and a drop-cast and annealed film (x_{FA} = 0.07, $x_{FA,\ actual}$ = 0.02). (b) Photoluminescence of x_{FA} = 0.00 spin-cast and annealed film, drop-cast and annealed film, and bulk crystals. (c) Overlay of the photoluminescence of different samples. The shift in the free exciton is indicated by a red arrow. All spectra were taken at excitation energy 3.95 eV and at 293 K; and all spin-cast films were annealed (see experimental section).

All materials grown slowly (drop-cast films, bulk crystals) exhibit **comparable amount of Ph-2**, consistent with slow growth being favorable to Ph-2. [4] The drop-cast x_{FA} = 0.00 film in **Figure S9b**

has an extra peak near 2.75 eV; this is likely a small amount of a non-n = 3 phase, as previously-discussed. [4] However, the emission trace follows closely that of the $(EA)_4Pb_3Br_{10}$, indicating that most of the emission from the drop-cast x_{FA} = 0.00 film comes from $(EA)_4Pb_3Br_{10}$. There is a gradual red shift in the free exciton energy for drop-cast films for the FA-containing films (**Figure S9c**, **Figure S7**) , likely due to changes to the lattice spacing and octahedral distortions [16] induced by the presence of FA-DMF in the interlayer. The free exciton remains distinct from Ph-1.

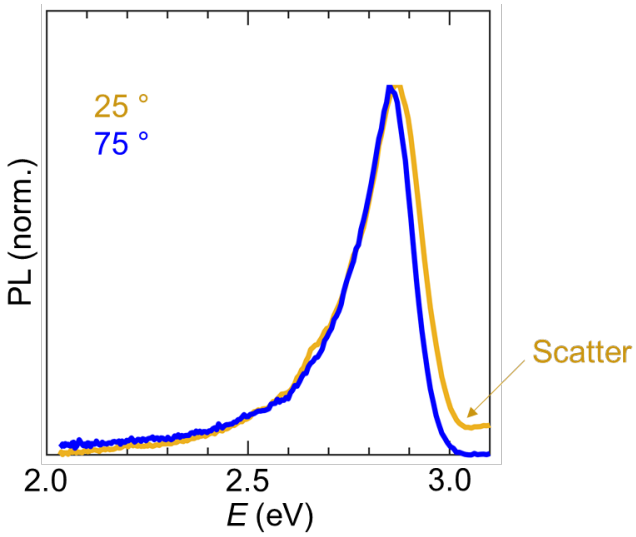

Figure S10. PL emission of a spin-cast x_{FA} = 0.07 film, taken by varying the angle the sample makes with the excitation and emission ports; excitation 3.95 eV at 293 K.

The relative emissive proportions of free excitons vs. lower-energy features can sometimes depend on the angle of the 2D semiconducting sheets with respect to the PL collection ("emission port" on fluorimeters). [6,8] For this reason, we varied the collection angle on the x_{FA} = 0.07 film, to see if the 2.7 eV feature would reappear. Traditionally, PL measurements are collected with films making a 45° angle with the emission port; here we used 25° and 75° to better probe the angle dependence of emission from the oriented 2D sheets. As shown in **Figure S10**, the emission does not change when rotating the film. A small extra amount of scattering appears when the sample is practically facing the excitation port (25°). We previously also verified that the relative proportions of different features do not change for $(EA)_4Pb_3Br_{10}$ films. [4]

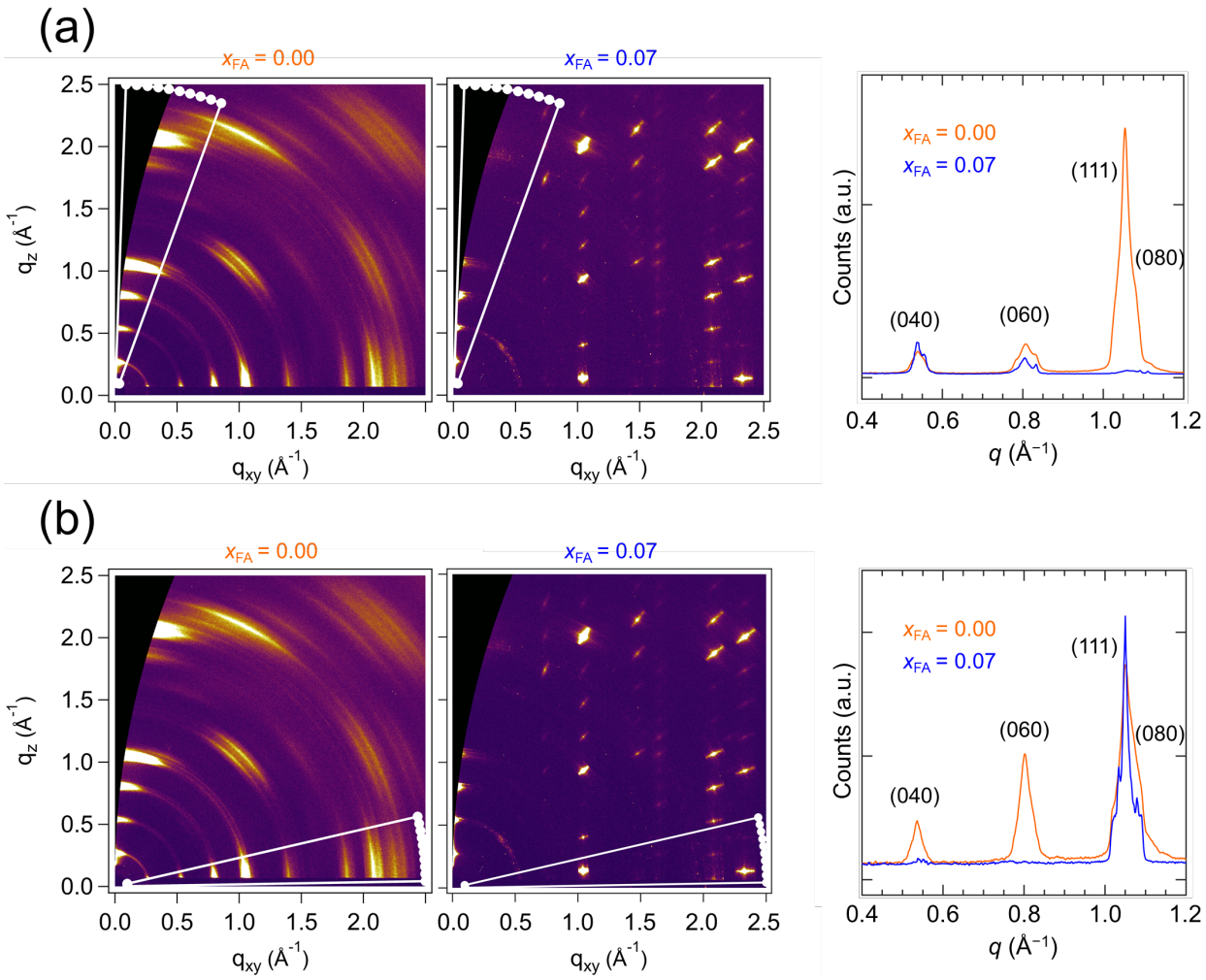

Figure S11. Integrated areas of GIWAXS patterns for spin-cast x_{FA} = 0.00 and 0.07 films, with the resulting patterns shown in the right panels. (a) near-out-of-plane integration, for an angle of 2-20 degrees from normal and (b) near-in-plane integration, for an angle of 77-89 degrees from normal.

The peaks near-out-of-plane (q_Z) are partially cut-off in GIWAXS (**Figure S11a**). For the spin-cast x_{FA} = 0.07 film, the (0k0) peaks are therefore better examined via XRD, which only probes q_Z. **Figure S4** confirms that the (0k0) peaks narrow significantly for x_{FA} = 0.07. From the near-in-plane integration (**Figure S11b**), the (111) peak can be decoupled into multiple sharp peaks, likely due to heterogeneity of locations of FA and DMF, which would inconsistently shift the lattice spacings. The sharpness of these peaks is consistent with peak narrowing observed above (**Figure S4**). No clear shift in q is observed with/without FA, consistent with XRD (**Figure S4**) and with only small amounts of FA and DMF being incorporated. In addition, with respect to size, FA < EA < DMF, so if FA and DMF are near each other, the lattice spacing might not change very much.

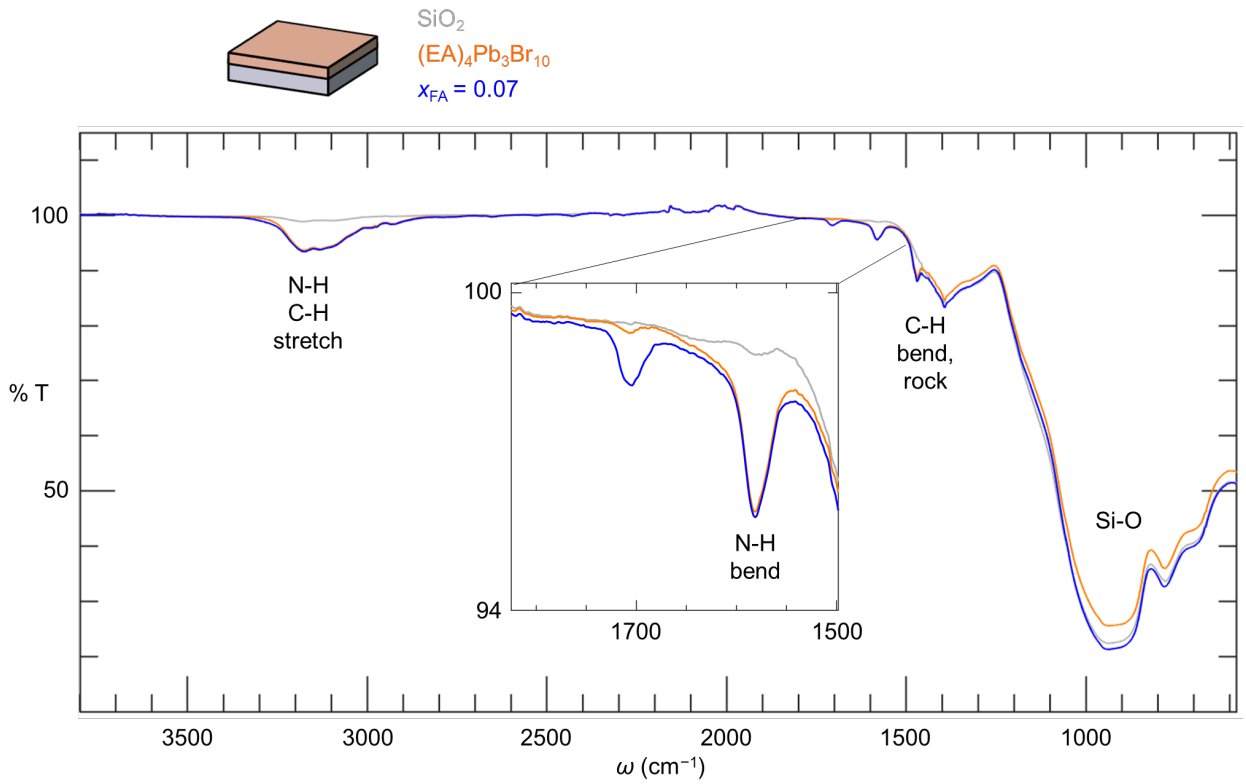

Figure S12. Full FTIR spectra of spin-cast films of x_{FA} = 0.00 ($(EA)_4Pb_3Br_{10}$) and x_{FA} = 0.07, and of the SiO_2 substrate. No PMMA capping layer was used. Spectra below 1500 cm^{-1} are dominated by the SiO_2 substrate.

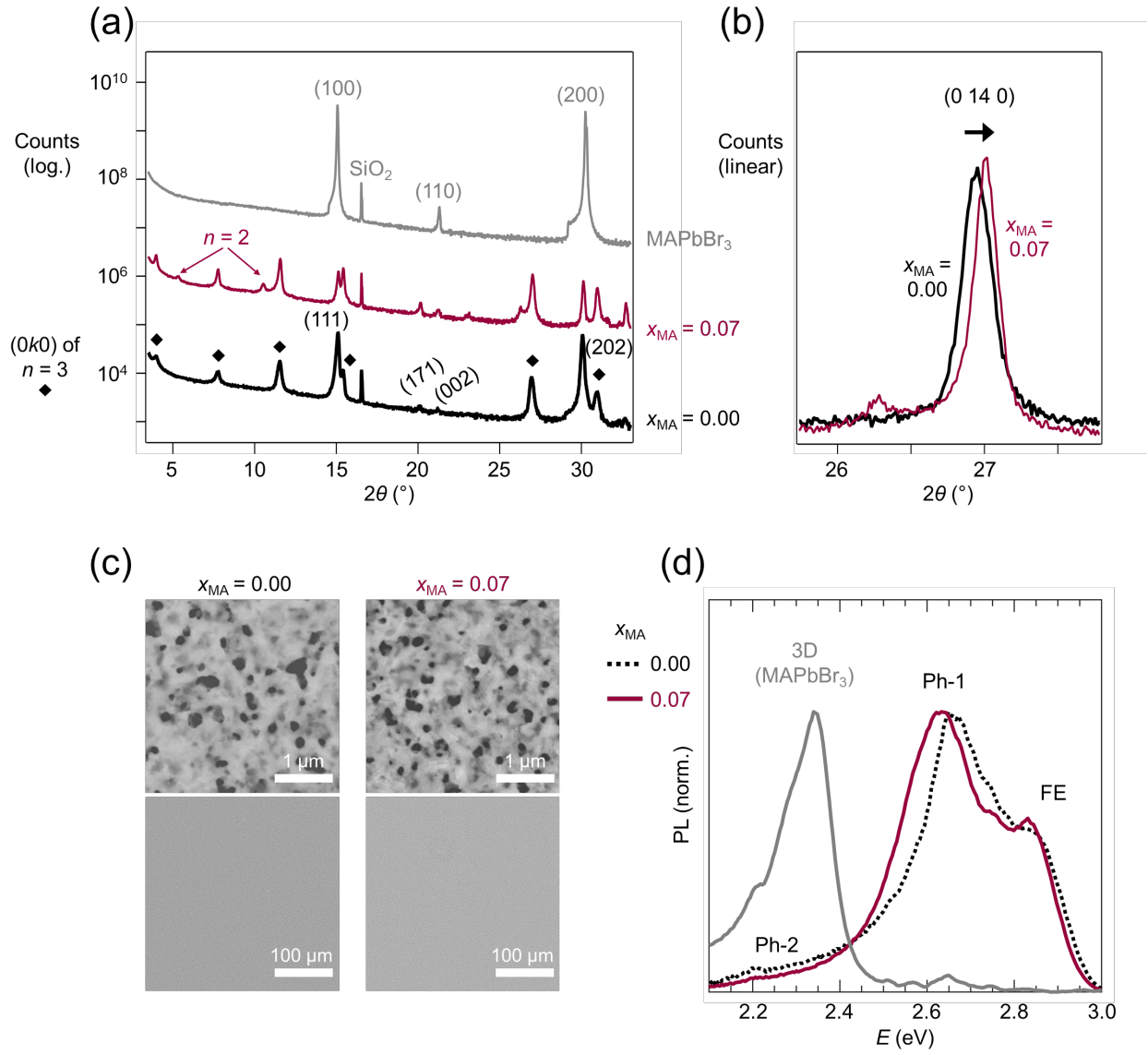

Figure S13. Structural and optical characterizations of spin-cast films with MA as the substituting cation (x_{MA} films), as well as of $MAPbBr_3$. (a) XRD patterns of x_{MA} = 0.00 and 0.07. The n = 3 peaks are indexed and visible for most patterns, with some that might be n = 2, by analogy with the $(BA)_2(MA)_{n-1}Pb_nI_{3n+1}$ RP films. (b) Closer look at the (0 14 0) peak from the n = 3 phase of both x_{MA} = 0.00 and 0.07. (c) SEM images of x_{MA} = 0.00 and 0.07. (d) Photoluminescence emission (3.94 eV excitation, 293 K). The free exciton and phonon-coupled peaks (Ph-1 and Ph-2) of the n = 3 phase are labelled. No other emission is visible. The emission of $MAPbBr_3$ is shown for comparison.

Examination of spin-cast x_{MA} = 0.07 films reveals that improvements to film growth, as well as the extinction of Ph-1, are specific to using FA.

Figure S13a shows that x_{MA} = 0.07 films retain the n = 3 structure in bulk, with some weak non-n = 3 peaks appearing. Based on analogy with the $(BA)_2(MA)_{n-1}Pb_nI_{3n+1}$ RP series, these extra peaks may be an n = 2 phase, with EA and MA as A-site cations. [9] Closer examination of the XRD patterns reveals a

lattice contraction of the n = 3 phase when MA is used (**Figure S13b**). This indicates that MA is likely in the A-site of the n = 3 phase, as MA is typically an A-site cation and not a spacer cation. In addition, the XRD peak intensities of x_{MA} = 0.07 and 0.00 are similar (**Figure S13b**), no improvements to domain size are seen (**Figure S13c**), and many pinholes are present in both films. Thus, using MA does not result in increases in domain size/homogeneous orientation of the 2D sheets, in contrast to what is observed when using FA (**Figure 4-5**).

Notably, using MA does not remove Ph-1. The emission spectra of x_{MA} = 0.07 and 0.00 are similar, and contain all three n = 3 peaks: the free exciton, Ph-1 and Ph-2. Using the smaller cation (MA) results in a slight red-shift of both the free exciton and Ph-1, consistent with slight lowering of octahedral distortions when smaller cations are in the A-site. [16] The retention of Ph-1contrasts strongly with the behavior of the FA compositions, for which the 2.7 eV feature disappears with x_{FA} = 0.07. Indeed, MA, with its sole ammonium group and position in the A-site, is likely not anchoring DMF in the spacer site.

The XRD pattern and photoluminescence emission of $MAPbBr_3$ are shown as confirmation that x_{MA} = 0.07 is not forming the (EA,MA)$PbBr_3$ alloy. [15] Typically, the presence of even very small amounts of a 3D phase results in carrier transfer to this 3D phase; and as a result, the emission spectrum is dominated by the 3D phase.[11] The strong presence of n = 3 emission and lack of a narrow peak near 2.3 eV confirm that x_{MA} = 0.07 does not contain the (EA,MA)$PbBr_3$ alloy.

References

[1] L. Mao, Y. Wu, C. C. Stoumpos, B. Traore, C. Katan, J. Even, M. R. Wasielewski, M. G. Kanatzidis, *J. Am. Chem. Soc.* **2017**, *139*, 11956.

[2] J. D. Dow, D. Redfield, *Phys. Rev. B* **1972**, *5*, 594.

[3] C. J. Dahlman, R. A. Decrescent, N. R. Venkatesan, R. M. Kennard, G. Wu, M. A. Everest, J. A. Schuller, M. L. Chabinyc, *Chem. Mater.* **2019**, *31*, 5832.

[4] K. et Al, .

[5] W. T. M. Van Gompel, R. Herckens, G. Reekmans, B. Ruttens, J. D'Haen, P. Adriaensens, L. Lutsen, D. Vanderzande, *J. Phys. Chem. C* **2018**, *122*, 4117.

[6] R. A. Decrescent, X. Du, R. M. Kennard, N. R. Venkatesan, C. J. Dahlman, M. L. Chabinyc, J. A. Schuller, *ACS Nano* **2020**, *14*, 8958.

[7] R. M. Kennard, C. J. Dahlman, J. Chung, B. L. Cotts, A. A. Mikhailovsky, L. Mao, R. A. DeCrescent, K. H. Stone, N. R. Venkatesan, Y. Mohtashami, S. Assadi, A. Salleo, J. A. Schuller, R. Seshadri, M. L. Chabinyc, *Chem. Mater.* **2021**, *33*, 7290.

[8] R. A. DeCrescent, N. R. Venkatesan, C. J. Dahlman, R. M. Kennard, X. Zhang, W. Li, X. Du, M. L. Chabinyc, R. Zia, J. A. Schuller, *Sci. Adv.* **2020**, 1.

[9] C. C. Stoumpos, D. H. Cao, D. J. Clark, J. Young, J. M. Rondinelli, J. I. Jang, J. T. Hupp, M. G. Kanatzidis, *Chem. Mater.* **2016**, *28*, 2852.

[10] W. L. Tan, Y. B. Cheng, C. R. McNeill, *J. Mater. Chem. A* **2020**, *8*, 12790.

[11] N. R. Venkatesan, R. M. Kennard, R. A. DeCrescent, H. Nakayama, C. J. Dahlman, E. E. Perry, J. Schuller, M. L. Chabinyc, *Chem. Mater.* **2018**, *30*, 8615.

[12] C. Liang, H. Gu, Y. Xia, Z. Wang, X. Liu, J. Xia, S. Zuo, Y. Hu, X. Gao, W. Hui, L. Chao, T. Niu, M. Fang, H. Lu, H. Dong, H. Yu, S. Chen, X. Ran, L. Song, B. Li, J. Zhang, Y. Peng, G. Shao, J. Wang, Y. Chen, G. Xing, W. Huang, *Nat. Energy* **2020**.

[13] R. Quintero-Bermudez, A. Gold-Parker, A. H. Proppe, R. Munir, Z. Yang, S. O. Kelley, A. Amassian, M. F. Toney, E. H. Sargent, *Nat. Mater.* **2018**, *17*, 900.

[14] I. Spanopoulos, I. Hadar, W. Ke, P. Guo, E. M. Mozur, E. Morgan, S. Wang, D. Zheng, S. Padgaonkar, G. N. M. Reddy, E. A. Weiss, M. C. Hersam, R. Seshadri, R. D. Schaller, M. G. Kanatzidis, **2021**.

[15] S. Gholipour, A. M. Ali, J. P. Correa-Baena, S. H. Turren-Cruz, F. Tajabadi, W. Tress, N. Taghavinia, M. Grätzel, A. Abate, F. De Angelis, C. A. Gaggioli, E. Mosconi, A. Hagfeldt, M. Saliba, *Adv. Mater.* **2017**, *29*, 1.

[16] Y. Fu, X. Jiang, X. Li, B. Traore, I. Spanopoulos, C. Katan, J. Even, M. G. Kanatzidis, E. Harel, *J. Am. Chem. Soc.* **2020**, *142*, 4008.

[17] N,N Dimethylformamide(68-12-2) 1H NMR, **2017**.